Journal of Materials Chemistry A

Orbital Chemistry of High Valence Band Convergence and Low-Dimensional Topology in PbTe

Journal:	*Journal of Materials Chemistry A*
Manuscript ID	TA-ART-02-2021-001273.R1
Article Type:	Paper
Date Submitted by the Author:	29-Mar-2021
Complete List of Authors:	Brod, Madison; Northwestern University, Materials Science and Engineering Snyder, G.; Northwestern University, Materials Science

Orbital Chemistry of High Valence Band Convergence and Low-Dimensional Topology in PbTe

Madison K. Brod[1] and G. Jeffery Snyder*[1]

[1] *Department of Materials Science and Engineering, Northwestern University, Evanston, Illinois 60208, USA. E-mail: jeff.snyder@northwestern.edu*

Abstract

The exceptional thermoelectric performance of PbTe is partially due to the high valley degeneracy, N_V, of the band edges. In this paper, we specifically look at the valence band (VB) structure of PbTe, which has been described using a 2-band model consisting of a light valence band with a maximum at the L-point in the first Brillouin zone and a heavy band with its maximum along the Σ-line. The light and heavy band extrema are located at low symmetry points, resulting in valley degeneracies of $N_V = 4$ and $N_V = 12$, respectively. The relative energy positions of the light and heavy valence bands can be tuned with temperature and defect concentration to make them effectively converged. In this study, analytical solutions from the tight-binding method are employed to understand the possible orbital interactions that that lead to this VB convergence. Both temperature and alloying based methods are explained as means to tailor the VB structure to achieve high valley degeneracy through band convergence. We predict five strategies for tuning valence band convergence: (i) alloying to introduce unfilled cation-s (s^0) defect states above valence band edge, (ii) increasing the lattice parameter through alloying or temperature, (iii) alloying to decrease the energy difference between anion-p and anion-s states, (iv) alloying to replace filled Pb-s (s^2) states with filled cation-s states that are lower in energy, and (v) decreasing the strength of anion spin-orbit interactions. Furthermore, we find that when the VBs are in a highly converged state, there is a topological transition in the electronic band structure to two-dimensional (2D) and potentially to one-dimensional (1D) character. Assuming acoustic-phonon scattering, we use the Boltzmann transport equation (BTE) to predict a significant enhancement in thermoelectric performance for the 2D and 1D band model, with a theoretical $zT > 10$ predicted for the 1D topology, ∼20 times greater than that predicted for the 3D topology. Although we specifically discuss PbTe, the qualitative results of this work can be applied to all the IV-VI, (IV = Ge, Sn, Pb; VI = S, Se, Te) rock salt compounds.

1 Introduction

1.1 Enhanced Thermoelectric Performance upon Band Convergence

Thermoelectric materials convert heat into electricity and vice-versa, making them candidates for waste-heat recovery and solid-state refrigeration, which could help in the development of clean and sustainable sources of energy and refrigeration.[1,2] For decades, thermoelectric materials such as PbTe[3] have been used by NASA in space-based applications. However, in order to achieve the widespread application of these materials for renewable energy generation and refrigeration, it is necessary to further optimize the thermoelectric figure of merit, given by $zT = S^2\sigma T/(\kappa_E + \kappa_L)$, where T is the temperature, S is the Seebeck coefficient, σ is the electrical conductivity, and κ_E and κ_L are the electronic and lattice contributions to the thermal conductivity, respectively.[2–10] As zT approaches infinity, the efficiency of a thermometric devices approaches the Carnot efficiency.[10]

The maximum achievable zT of a thermoelectric material increases as its thermoelectric quality factor, B, increases (see Eqs. B27-B29 in Appendix B). The quality factor is proportional to the weighted mobility, μ_w, (see Eqs. B9 and B30 in Appendix B) which can be expressed as $\mu_w = \mu_0(m^*_{DOS}/m_e)^{3/2}$, where μ_0 is the mobility parameter of the carriers, m^*_{DOS} is the density of states (DOS) effective mass, and m_e is the free electron mass. The DOS effective mass can be expressed as $m^*_{DOS} = N_V^{2/3} m^*_b$, for a multi-valley electronic structure where N_V is the band or valley degeneracy, and m^*_b is the DOS effective mass for each valley.[6,9,11–15] Therefore the quality factor, B, is proportional to the valley degeneracy, so increasing N_V (without substantially increasing inter-valley scattering) enhances the performance of a thermoelectric material. In this work, we focus on two primary methods to achieving high valley degeneracy. The first method is having band extrema at low symmetry points in the Brillouin zone (BZ) of high symmetry crystal structures when there is no (or limited) inter-valley scattering.[11,16–19] Lower-symmetry points map onto multiple symmetrically equivalent points, providing more pathways for carrier transport. For instance, an extrema at a point with 6 symmetrically equivalent points in the BZ would have a degeneracy of $N_V = 6$.[20] The second method involves converging multiple band extrema within a few k_BT in energy at different (or the same) points in the BZ.[4,16,21]

Additionally, it has been predicted that reducing the dimensionality of thermoelectric materials significantly improves thermoelectric performance.[22–24] Traditionally, low-dimensional behavior is achieved by designing nano-scale materials that confine electronic transport in at least one direction.[25–27] That being said, when multiple bands contribute to transport, this type of low-dimensionality that leads to quantum confinement can actually reduce thermoelectric performance by breaking degeneracy.[28,29] However, low-dimensional transport has been observed in bulk three-dimensional (3D) materials that have 2D Fermi surfaces.[22,24,30] Gains in thermoelectric performance are observed in these bulk materials with low-dimensional electron bands, providing novel pathways to achieve the efficiency gains associated with low-dimensionality without the challenges and costs associated with synthesizing nano-scale or nano-structured material or the loss in thermoelectric

power from degeneracy-breaking quantum confinement effects.[22,24]

1.2 Convergence Behavior in PbTe Valence Bands

For several decades, PbTe has been one of the highest performing thermoelectric materials, reaching $zT > 1$ for certain alloys.[4,21,31–34] PbTe and the similar SnTe and GeTe based alloys have been employed as a power source for NASA space missions since the 1960's[3,35]. PbTe has a direct bandgap at the L-point in the BZ, which has a degeneracy of $N_V = 4$,[4,16,21,33,36,37] and inter-valley scattering is symmetry-forbidden at the L-point[11,18,19]. Another crucial feature of the PbTe VBs is that there is a secondary valence band along the Σ symmetry line, which is found experimentally to be ∼0.1-0.2 eV below the L band maximum (at low temperature).[4,38]

The maximum along Σ is at an even lower symmetry point and has a valley degeneracy of $N_V = 12$.[4,34–36,39–42] As temperature increases, the energy of the L VBM decreases relative to that of the Σ VBM, causing the bands extrema to approach each other in energy.[4,16,38,40,41] The two bands converge at T ∼700 K, resulting in an exceptionally high valley degeneracy[4,16,16,21,32–34,38,41,43–46] with an effective $N_V > 12(\Sigma) + 4(\mathrm{L}) = 16$, likely in the range of $N_V \sim 30$ to $N_V \sim 70$.[46] DFT calculations suggest that there is a topology change when the two VBs are converged and the Σ pockets merge into the L pockets forming threads or tubes, leading to 2D electron bands in 3D PbTe (and the other lead chalcogenides).[24,40,46]

The convergence of the valence band (VB) carrier pockets in PbTe can also be tuned by alloying with various substitutions.[4,8,21,32,35,36,47–50] For instance, alloying PbTe with PbSe, decreases the energy of the secondary VBM along Σ relative to the primary VBM along L.[4] By contrast, cation-site alloying with impurities, such as Cd, Mg, Mn, Na, Sr, and Hg—all of which introduce s^0 states above VB edge—increases the energy of the Σ-band relative to the L band.[8,16,21,32,35,47–50]

Here, we develop analytical tight-binding (TB) solutions that describe the relative positions of the L and Σ VB extrema in rock salt PbTe. We find that the Σ VB forms because of nearly the same but weaker interactions as the L band. We extend this TB analysis discuss the relative positions and convergence of two additional VBs, one with a maximum along the Δ symmetry line and one with a maximum at W. Using these solutions, we predict trends in the VB convergence behavior with respect to various orbital interactions and use them to understand the role of temperature and alloying in achieving high convergence. We find a topological transition in the TB electronic structure, regardless of which TB parameters were tuned to achieve convergence, of PbTe from a 3D topology to 2D and even 1D topologies when the VBs are in a highly converged state.

The evolution of the Fermi surface topology of lead chalcogenides and the corresponding trends in thermoelectric performance are summarized in Fig. 1. We show idealized sketches of the valence band Fermi surfaces corresponding to various topologies. The 3D topology is characterized by ellipsoidal pockets (Fig. 1a) at L. As the bands become more converged, heavier pockets form at the Σ band maximum (Fig. 1b). Eventually, the L and Σ pockets converge completely to to form

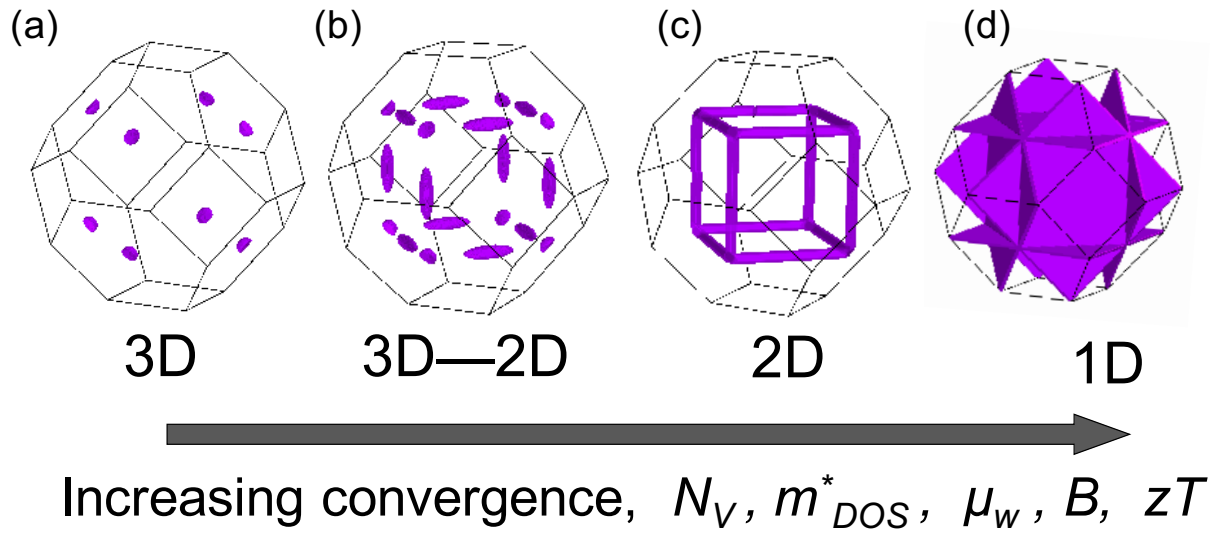

Figure 1: Evolution of the PbX (X = S, Se, Te) valence band Fermi surface topology and enhancement in the thermoelectric performance upon increased band convergence.(a) The least-converged 3D Fermi surface is characterized by four ellipsoidal pockets centered at the L-points. (b) As the bands become more converged, elongated heavy ellipsoidal pockets form at the Σ maximum. (c) The 2D topology resembles 12 tubes, simplified as cylinders. (d) The 1D Fermi surface resembles 6 sheets with a finite thickness. As the Fermi surface evolves from (a)-(d), the valley degeneracy (N_V), density of states mass (m^*_{DOS}), weighted mobility (μ_w), thermoelectric quality factor (B), and thermoelectric figure of merit (zT) all increase.

tubes (or threads) corresponding to a 2D topology (idealized as cylinders forming the edges of a cube with side length $2\pi/a$ in Fig. 1c). As discussed later, these tubes are actually bent towards the center of the cubic face. Finally, as additional VB pockets at W and along Δ converge with the L and Σ pockets, with the tuning of spin-orbit interactions, the Fermi surface evolves into sheets (Fig. 1d), which are indicative of 1D-type transport.

Furthermore, we use the effective mass model to compare the topological electronic states of PbTe and predict substantial thermoelectric performance gains in lower-dimensional topologies, with a predicted theoretical maximum ∼ 20 times greater for the 1D topology of the highly converged VBs without SOC than for the 3D ellipsoidal topology. This enhancement can be attributed to large increases in the effective valley degeneracy to $N_V \sim 180$ for the 2D topology and to $N_V \sim 2600$ for the 1D case. Finally, we propose alloying-based design strategies to achieve these highly converged, low-dimensional topologies. The qualitative results of this analysis are also applicable to the other Group IV chalcogenides (GeTe, SnTe, PbSe and PbS).[51–55]

2 Background — Tight-Binding Model for PbTe

The tight-binding (TB) method, also described as the linear combination of atomic orbitals (LCAO), is a chemically intuitive method for approximating the electronic structure of materials, with the

significant advantage of extremely short computational times. The TB method employs an orthonormal basis of atomic orbitals (s, p, d, etc.) and can be described by a set of overlap parameters, which are related to the hopping integrals that comprise the TB Hamiltonian.[56–61] They describe the strength of interactions between pairs of atomic orbitals and whether they are bonding or antibonding in nature. These parameters are approximately related to the interatomic spacing through the relationship $\sim 1/d^2$, where d is the interatomic spacing between neighboring orbitals. In general, these overlap parameters are expressed in the form $V_{\alpha\beta m}$, where α and β denote the orbitals interacting and m denotes the type of bonding (σ, π, etc).[56,59–61] Here, we use four types of these overlap parameters to describe the nature and strength of the orbital interactions in PbTe, $V_{ss\sigma}$, $V_{sp\sigma}$, $V_{pp\sigma}$, and $V_{pp\pi}$. These describe the of s–s σ-bonding, s–p σ-bonding, p–p σ-bonding, and p–p π-bonding, respectively. We consider all of these interaction types for both nearest neighbor (anion-cation) and next-nearest neighbor (anion-anion or cation-cation) interactions, giving a total of 13 overlap parameters.[62] The sign of the parameter determines whether the interaction is bonding (negative) or anti-bonding (positive) in nature at Γ.[61]

In this work, the TB analytical solutions describing the VB edge in PbTe are reminiscent of the simple quantum mechanical solution for the bonding and anti-bonding in a diatomic molecule. Consider a diatomic molecule, MX with an energy level diagram depicted in Fig 2a. The on-site energy for a M-atom cation orbital, E_M, is the energy of the atomic orbital. Similarly the on-site energy for the anion X orbital is E_X. The overlap parameter describing the interaction of these two orbitals is V_{MX}. Note that this simple diatomic molecule model is generalized to account for the bonding between any types of orbitals. When M and X bond, they form a bonding (E_{MX-}) state (having stronger X than M character) and an antibonding (E_{MX+}) state (having stronger M character) with energies approximately described by Eq. 1.[61,63] The energy E_{MX-} or E_{MX+} relative to the average of the two on-site energies ($|E_{MX\pm} - \frac{1}{2}(E_M + E_X)|$) can be described by the hypotenuse of a right triangle with legs A and V as seen in Fig. 1b.

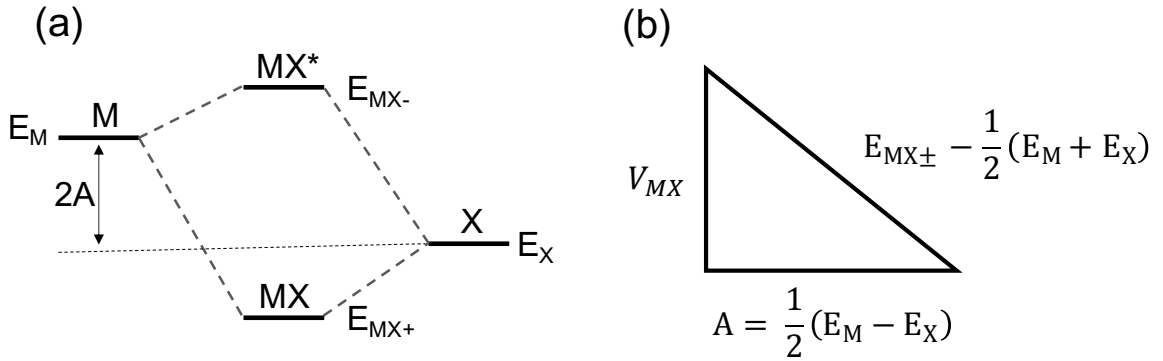

Figure 2: (a) Simple energy level diagram for a heteropolar diatomic molecule MX. The energy difference between the cation state M and the anion state X is given by 2A. (b) The energy difference for the bonding and antibonding states relative to the average value of the onsite energy in a diatomic molecule can be described by a right triangle.

$$E_{MX\pm} = \frac{1}{2}\left(E_M + E_X\right) \pm \frac{1}{2}\sqrt{\left(E_M - E_X\right)^2 + 4V_{MX}^2} \quad (1)$$

The plus (+) solution describes the anti-bonding state, and the minus (-) solution describes the bonding state. If $V_{MX} = 0$, then the solutions are simply the on-site (unchanged atomic) energies. If $E_M = E_X$ (homopolar covalent bond) the change in energy is simply V_{MX}.

A TB model developed by fitting the TB parameters to Density Functional Theory (DFT) calculations of the PbTe electronic band structure using the Perdew-Burke-Ernzerhof (PBE)[64] functional has been used to understand the orbital interactions that explain the location of the VBM and the shape of the VB edge in PbTe. The results along with the methods used to develop the TB model in this paper are described elsewhere.[62] In PbTe, the upper three VB states consist primarily of Te-p character. Below the Te-p valence bands is a distinct Pb-s band, and below this is a Te-s band. At the L-point, there is a repulsive, or antibonding, interaction between the Te-p states and the Pb-s states below them, pushing the Te-p states at the VB edge higher in energy and resulting in a energy maximum there.[8,24,62,65–67]

3 Results and Discussion

3.1 Analytical Tight-Binding Solutions

Using an 8-dimensional TB basis consisting of the Pb-6s, Pb-6p_x,p_y,p_z, Te-5s, and Te-5p_x,p_y,p_z, analytical expressions for the eigenvalues of the TB Hamiltonian are determined and are used to derive an analytical approximation describing the VB convergence. The analytical form of the TB Hamiltonian used to determine these solutions is described in Appendix A. Spin-orbit coupling (SOC) effects are not considered when deriving the analytical expressions but are discussed later, numerically. The size of the basis would be doubled (16-dimensional) to account for SOC effects.

In order to determine an analytical expression that describes the convergence, we define a point Σ' in the BZ that is located exactly 2/3 along the $\Gamma - K$ symmetry line at $\Sigma' = (\pi/a, \pi/a, 0)$, where a is the lattice constant. This point represents the approximate location of the Σ VBM and has many of the same interactions as found at $\mathrm{L} = (\pi/a, \pi/a, \pi/a)$. The true, numerical value of the Σ maximum is denoted as Σ^* in this paper, and its exact location varies based on the parameters used in the calculation. There are 12 symmetrically equivalent Σ' points in the first BZ for the rock salt structure. Although the exact location of the secondary VBM along Σ varies with temperature and composition, it is generally located at approximately this point in the TB model, so this point is chosen to help evaluate approximate analytical solutions. There are also maxima located along Δ symmetry line ($N_V = 6$) and at the W-point ($N_V = 6$). The maxima along the Δ is found at a point $\sim 4/9$ along the Δ-line ($\Gamma - X$) and is denoted by Δ^* throughout this paper. Like Σ^*, its location is not constant. However, for the sake of analytically describing the Δ band and the interactions responsible for its maximum, we define a point, denoted Δ', halfway along Δ at

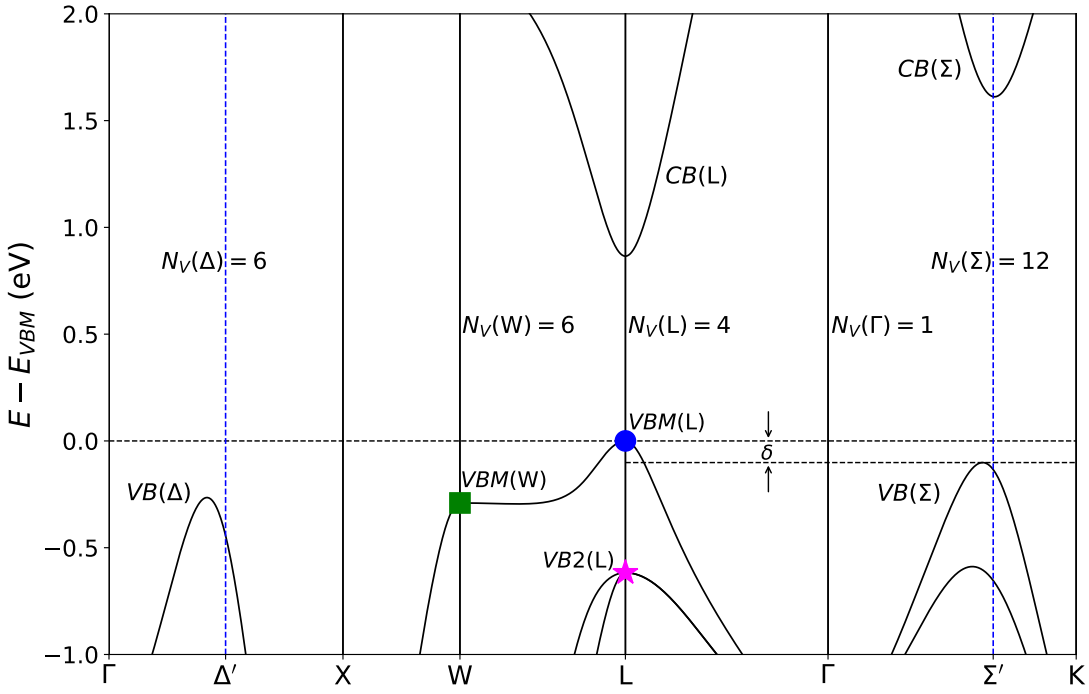

Figure 3: Labeled PbTe electron bands calculated using the TB model without SOC. The local valence band maxima (VBMs), valence bands (VBs) along Δ and Σ, conduction bands (CBs) at L and along Σ, and valley degeneracies (N_V) are labeled. The energy of the VBM at L is labeled with a blue circle, the energy of the VBM at W is labeled with a green square, and the two degenerate VBs below the VBM at L is labeled with a magenta star. δ is shown as the energy difference between the VBM at L and the VBM along Σ.

$\Delta' = (\pi/a, 0, 0)$. There are 6 symmetrically equivalent Δ^*– and Δ'–points in the first BZ. The maxima are labeled in Fig. 3, along with their valley degeneracies and additional values of interest for analyzing the band structure. A labeled diagram of the first BZ that shows the location Σ' and Δ' can be seen in Fig. D1 in Appendix D.[68] The DFT-PBE (no SOC) band structure for this same path and energy window can be seen in Fig. S5 of the Supporting Information.

The parameter, δ, is defined as the difference in energy between the primary and secondary VBMs located at L and along Σ (at Σ^*), respectively, where E_{VBM}(L) (shown with a blue circle in Fig. 3) is the energy of the L VBM, and $E_{VBM}(\Sigma^*)$ is the energy of the (true) Σ VBM, the exact location of which varies. It can be expressed through the equation, $\delta = E_{VBM}$(L) $-E_{VBM}(\Sigma^*)$, and is shown in Fig. 3. We use δ as a proxy for the VB convergence. Therefore, if E_{VBM}(L)> $E_{VBM}(\Sigma^*)$, a decrease in δ corresponds to greater VB convergence. In order to determine an analytical approximation for δ, analytical expressions for the valence band eigenvalues (energies) of the TB Hamiltonian at both L and near the Σ VBM are determined.

At the L-point, the eigenvalue representing the light band extrema are described by Eqs. 2-3.

$$E_{VBM}(\mathrm{L}) = \frac{1}{2}\left(E'_{p,Te}(\mathrm{L}) + E_{s,Pb}\right) + \frac{1}{2}\sqrt{\left(E'_{p,Te}(\mathrm{L}) - E_{s,Pb}\right)^2 + 48V_{sp\sigma}^2} \quad (2)$$

$$E'_{p,Te}(\mathrm{L}) = E_{p,Te} + 4V_{pp\pi,Te} - 4V_{pp\sigma,Te} \quad (3)$$

$E_{s,Pb}$ is the on-site energy of the Pb-s state, $E_{p,Te}$ is the Te-p onsite energy term, and $V_{sp\sigma}$ here denotes the σ-bonding TB parameter that describes the interaction between the Pb-s and Te-p orbitals. $V_{pp\pi,Te}$ and $V_{pp\sigma,Te}$ describe the Te-p–Te-p π- and σ-bonding interactions, respectively. Note that Eq. 2 has a form similar to that given in Eq. 1 describing a heteropolar diatomic molecule. From these equations, we can see that the VBM at L is primarily from Te-p orbitals (aligned along [111]), which are increased in energy from repulsive antibonding interactions with its 6 nearest-neighbor Pb-s states. There is also a slight reduction in energy due to next-nearest neighbor σ- and π-bonding interactions with the Te-p orbitals. We will see a similar correspondence to the diatomic molecule model at the other VBM points, which will be discussed in more detail later.

The other two degenerate valence band states at L (below the VBM state), denoted $E_{VB2}(\mathrm{L})$ and shown with a magenta star in Fig. 3, are described by the analytical solution expressed in Eq. 4, with no net $V_{sp\sigma}$ interaction.

$$E_{VB2}(\mathrm{L}) = E_{p,Te} + 2V_{pp\sigma,Te} - 2V_{pp\pi,Te} \quad (4)$$

The solution at L is an exact eigenvalue solution to the TB Hamiltonian without SOC. However, the solution at Σ' is not as simple and can only be approximated. If we ignore the relatively weak Te-s/Te-p interactions, the analytical approximation for the Σ', or heavy-band, maximum can be expressed in Eqs. 5-6.

$$E_{VBM}(\Sigma') = \frac{1}{2}\left(E'_{p,Te}(\Sigma') + E_{s,Pb}\right) + \frac{1}{2}\sqrt{\left(E'_{p,Te}(\Sigma') - E_{s,Pb}\right)^2 + 32V_{sp\sigma}^2} \quad (5)$$

$$E'_{p,Te}(\Sigma') = E_{p,Te} - 2V_{pp\sigma,Te} + 2V_{pp\pi,Te} \quad (6)$$

$E'_{p,Te}(\Sigma')$ like $E'_{p,Te}(\mathrm{L})$ is essentially an adjusted on-site energies that results from anion–p interactions. Here, we see that the character of the VBM at Σ' is very similar to that at L. Both exhibit primarily Te-p character with antibonding interactions with Pb-s (slightly weaker at Σ than at L) and some Te-Te next-near neighbor p—p bonding interactions.

The TB interaction between the Te-s and Te-p states, described by the TB parameter, $V_{sp\sigma,Te}$, is not entirely negligible when studying the VB structure. We do not go into details here, but it can be shown that increasing $V_{sp\sigma,Te}$ and decreasing the energy difference between the Te-p and

Te-s states would increase $E_{VBM}(\Sigma')$ relative to $E_{VBM}(\mathrm{L})$. This trend is related to the fact that the Te-p orbital comprising the VBM along Σ is antibonding with its next-nearest neighbor Te-s orbitals, while the Te-p state at the L VBM is non-bonding with these Te-s orbitals.

Eqs. 2 and 5 show that the L VBM has a greater dependence on $V_{sp\sigma}$ than the Σ VBM, so we expect increasing the magnitude of $V_{sp\sigma}$ to increase the separation between the light and heavy VB band extrema (when $E_{VBM}(\mathrm{L}) > E_{VBM}(\Sigma)$). Additionally, the dependence of the Σ band energy on $V_{sp\sigma,Te}$ indicates that strengthening the anion s-p interactions would increase the Σ VB relative to the L band. With regards to the next-nearest neighbor anion-p interactions (σ and π), The L band has a stronger dependence on the Te p–p interactions, but at both the L and Σ maxima, they decrease the band edge energy as they increase in strength.

We introduce a new parameter, δ', which represents an approximation for δ using the analytical expressions or approximations for $E_{VBM}(\mathrm{L})$ and $E_{VBM}(\Sigma')$. To evaluate δ', we ignore $V_{sp\sigma,Te}$ for simplicity, so δ' can be expressed through Eq. 7. The parameter $V_{pp,Te}$ represents the combined strength of the π- and σ-bonding between next-nearest neighbor anion-p interactions and can be expressed as $V_{pp,Te} = V_{pp\sigma,Te} - V_{pp\pi,Te}$. $V_{pp\pi,Te}$ is always less than zero, and $V_{pp\sigma,Te}$ is greater than zero, so $V_{pp,Te}$ is strictly a positive value. The parameter, A, represents half of the energy difference between the anion-p and cation-p states and can be expressed as $A = \frac{1}{2}(E_{p,Te} - E_{s,Pb})$.

$$\delta' = -V_{pp,Te} + \left[\sqrt{(2A - 4V_{pp,Te})^2 + 48V_{sp\sigma}^2} - \sqrt{(2A - 2V_{pp,Te})^2 + 32V_{sp\sigma}^2}\right] \tag{7}$$

Finally, we solve for the value of $V_{sp\sigma}$ at which $\delta' = 0$ in order to approximate the value at which maximum convergence of the light and heavy VBs can theoretically be achieved, according to the TB model. The value of $V_{sp\sigma}$ at which the L- and Σ-bands are exactly converged is denoted as $V_{sp\sigma}^*$ and expressed in Eq. 8. The energy of the valence band extrema at this point, E_{VBM}^*, is expressed in Eq. 9.

$$V_{sp\sigma}^* = \sqrt{AV_{pp,Te} + V_{pp,Te}^2} \tag{8}$$

$$E_{VBM}^* = E_{p,Te} + 2V_{pp,Te} \tag{9}$$

We can rearrange Eq. 8 to find the critical convergence value of any of the three parameters. For instance, $A^* = \frac{1}{2}(E_{p,Te} - E_{s,Pb}) = (V_{sp\sigma}^2 - V_{pp,Te}^2)/V_{pp,Te}$. The converged state is the same regardless of which parameter is tuned to its critical value to achieve the convergence. One crucial observation from this derivation is that the approximated maximum energy of both the converged light and heavy VBs is equivalent to the energy of the doubly degenerate VB states below the VBM at L when $V_{sp\sigma} = V_{sp\sigma}^*$, or when $A = A^*$. That is $E_{VBM}^* = E_{VB2}$, so for cases where SOC interactions are minimized, multiple bands would have the same energy, leading to higher effective band degeneracy than can be obtained from only the convergence of the L and Σ maxima alone.

We also obtain an analytical approximations for the W= $(\pi/a, 2\pi/a, 0)$ and Δ VBMs, as their convergence behavior is critical for understanding topological transitions in the PbTe Fermi surface discussed later. The eigenstate of the W VBM, $E_{VBM}(\mathrm{W})$, (labeled with a green square in Fig. 3) without SOC is expressed in Eqs. 10-12, where $V_{ss\sigma,Pb}$ is the overlap parameter describing the σ-bonding interactions between the next-nearest neighbor Pb-s orbitals.

$$E_{VBM}(\mathrm{W}) = \frac{1}{2}(E'_{p,Te}(\mathrm{W}) + E'_{s,Pb}(\mathrm{W})) + \frac{1}{2}\sqrt{(E'_{p,Te}(\mathrm{W}) - E'_{s,Pb}(\mathrm{W}))^2 + 16V_{sp\sigma}^2} \tag{10}$$

$$E'_{p,Te}(\mathrm{W}) = E_{p,Te} - 4V_{pp\pi,Te} \tag{11}$$

$$E'_{s,Pb}(\mathrm{W}) = E_{s,Pb} - 4V_{ss\sigma,Pb} \tag{12}$$

Based on this solution, we expect the energy of the VB edge at W to increase with $V_{sp\sigma}$ and to decrease with increasing A.

Finally, we can approximate a solution at Δ' (1/2 along Δ), by ignoring the Te-p/Pb-p interactions and simply studying the Te-p/Pb-s interactions along with the next-nearest neighbor interactions. The approximation for the TB eigenvalue corresponding to the VB edge at Δ' is described through Eqs. 13 – 16.

$$E_{VBM}(\Delta') = \frac{1}{2}(E''_{p,Te}(\Delta') + E'_{s,Pb}(\Delta')) + \frac{1}{2}\sqrt{(E''_{p,Te}(\Delta') - E'_{s,Pb}(\Delta'))^2 + 16V_{sp\sigma}^2} \tag{13}$$

$$E''_{p,Te}(\Delta') = \frac{1}{2}(E'_{p,Te}(\Delta') + E'_{s,Te}(\Delta')) + \frac{1}{2}\sqrt{(E'_{p,Te}(\Delta') - E_{s,Te}(\Delta'))^2 + 128V_{sp\sigma,Te}^2} \tag{14}$$

$$E'_{p,Te}(\Delta') = E_{p,Te} + 4V_{pp\pi,Te} \tag{15}$$

$$E'_{s,Te}(\Delta') = E_{s,Te} + 4V_{ss\sigma,Te} \tag{16}$$

$V_{sp\sigma,Te}$ is the overlap parameter between the next-nearest neighbor Te-p and Te-s orbitals. We do not give the solution for $E''_{s,Pb}$, in Eq. 13, but it is a correction to the Pb-s on-site energy at Δ' that takes into consideration the Pb-s/Pb-p and Pb-s/Pb-s interactions at this point. The dependence on $V_{sp\sigma}$ at Δ' is the same as it is at W. We also expect the repulsive Te-s/Te-p interactions to further increase the energy of the Δ VBM.

If only the interaction between the Te-s and Pb-p orbitals is taken into account (all overlap parameters except for $V_{sp\sigma}$ are set to zero), then the Δ VBM would be located at exactly Δ', and the Σ maximum would be located at exactly Σ'. It is the second order interactions that cause the location of the maximum in k-space to vary off these points, the Δ maximum slightly towards Γ and the Σ maximum slightly closer to 1/2 instead of 2/3 along the Γ-K path.

3.2 Comparison to Diatomic Molecules

Eqs. 2, 5, 10, and 13 all describe the relationship of the energy of the VB extrema with respect to the interaction between the Pb-s and Te-p states, quantified by $V_{sp\sigma}$. We observe that these equations have a form analogous to that describing the anti-bonding state in a diatomic molecule bond (described by the TB model) depicted in Fig. 2. Comparing Eq. 1 to Eqs. 2, 5, 10, and 13, we can obtain an effective diatomic overlap parameter, V_D, for each VB extrema. At the L-, Σ'-, W-, and Δ'-points we obtain $V_D(\mathrm{L}) = 2\sqrt{3}V_{sp\sigma}$, $V_D(\Sigma') = 2\sqrt{2}V_{sp\sigma}$, $V_D(\mathrm{W}) = 2V_{sp\sigma}$, and $V_D(\Delta') = 2V_{sp\sigma}$, respectively. The pre-factor in front of $V_{sp\sigma}$ in each of these expressions represents the effective number of s-p σ-bonds contributing to the energy of the VB extrema. In order to relate this to an orbital bonding picture of the VB state, it is instructive to rewrite these expressions as follows:

$$V_D(\mathrm{L}) = 6 \times \frac{1}{\sqrt{3}} \times V_{sp\sigma} \tag{17}$$

$$V_D(\Sigma') = 4 \times \frac{1}{\sqrt{2}} \times V_{sp\sigma} \tag{18}$$

$$V_D(\mathrm{W}) = 2 \times 1 \times V_{sp\sigma} \tag{19}$$

$$V_D(\Delta') = 2 \times 1 \times V_{sp\sigma} \tag{20}$$

In general, we can write Eqs. 17-20, in the following form.

$$V_D = N \times l \times V_{sp\sigma} \tag{21}$$

In Eq. 21, N is the net number of anti-bonding interactions, and l is the cosine projection of the vector between the Γ-point and the relevant k-point along the orientation of the p-orbital σ-bonding axis. The p-orbital referenced here is the one that contributes to the eigenstate of the highest VB. The other two p-orbitals would correspond to the two lower VBs. The value of N in Eqs. 17–21 can be visually determined (Fig. 4) as the number of bonding or antibonding configurations between the Te-p orbital and the nearest neighbor Pb-s orbitals. Each Te-p orbital

is surrounded by 6 nearest neighbor Pb-s orbitals. At the Γ-point, the Pb-s and Te-p orbitals are oriented such that half of the interactions are bonding, and half are antibonding, yielding zero net-bonding between the Te-p and Pb-s orbitals,[62] as seen in Fig. 4a. Therefore, at Γ we would have $V_D(\Gamma) = 0$. The p_x, p_y, and p_z orbitals at the Γ–point are degenerate, so an equivalent picture can be drawn for all three of these p-orbital orientations, but for simplicity only the p_x orbital is shown. Applying phase changes to the orbitals for the other relevant k-points of interest, we can count the number of bonding/anti-bonding interactions.[58]

At Δ', the k vector is along the [100] direction, so the p-orbital is aligned along the direction toward the Pb-s orbital (x), giving a cosine projection of $l = 1$. The phase of one of the neighboring Pb-s states along this direction flips, so 2 of the neighboring Pb atoms have s-orbitals in an anti-bonding configuration with the Te-p orbital (Fig. 4b). A similar Pb-s orbital configuration relative to the Te-p orbital can be drawn at W, but multiple repeat units would be required to show the full symmetry of the orbital phases. At Σ', the phases of the Pb-s orbitals along 2 of the 3 Cartesian directions alternate, resulting in 4 of the Pb-s orbitals being in an antibonding configuration with the Te-p orbital (Fig. 4c). The VBM p-orbital at this point is aligned in the [110] direction, yielding $l = 1/\sqrt{2}$ and effectively weakening the interaction. Finally, at the L-point, the phases of the Pb-s orbitals alternate in all three directions such that the Te-p orbital is anti-bonding with all 6 of the nearest-neighbor Pb-s orbitals (Fig. 4d). The VBM p-orbital is aligned such that it is parallel to the [111] direction, giving in $l = 1/\sqrt{3}$.

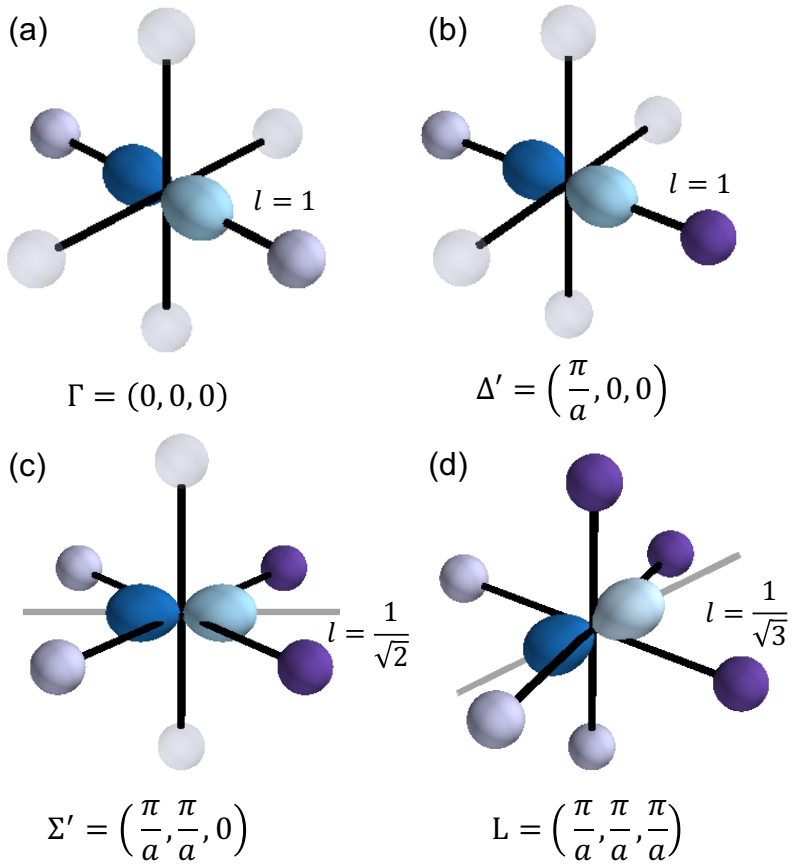

Figure 4: Representation of the orbital configurations of the highest energy Te-p orbital (making up the valence band maximum) surrounded by 6 nearest-neighbor Pb-s orbitals in an octahedral coordination at (a) Γ, (b) Δ', (c) Σ', and (d) L. Blue coloring is used for the Te-p orbitals and purple coloring is used to show the Pb-s orbitals. The light and dark shading represents the + or - phase of the orbital. The cosine projection between the p-orbital and the x-axis, l is labeled for each case. The Pb-s orbitals that are separated from the Te-p orbital by a vector that is entirely orthogonal to the Te-p orbital's σ-bonding axis are shaded with a lower opacity to represent the fact that they are non-bonding with the Te-p orbital shown.

3.3 Trends in the Convergence Behavior of PbTe Valence Bands

Using Eqs. 2 and 5, the analytical trends of δ' with respect to A, $V_{sp\sigma}$, and $V_{pp,Te}$, normalized to their initial values (used to produce Fig. 3), are plotted in Fig. 5. When all the parameters are at their initial values, δ' is approximately 0.2 eV. The bands become more converged ($\delta' \to 0$) as $V_{pp,Te}$ and A increase and as $V_{sp\sigma}$ decreases. The decrease of δ' with $V_{pp,Te}$ indicates that strengthening interactions between the next-nearest neighbor Te-p orbitals increases the convergence of the heavy and light VB pockets. Furthermore, both the increase of δ' with $V_{sp\sigma}$ and the decrease of δ' with A, suggest that stronger cation-anion s–p interactions decrease convergence when the cation-s states are lower than the anion-p states.

Next, we perform a series of virtual "experiments" (or thought experiments) to better understand qualitatively the evolution of the VB structure upon the variation of several TB parameters.

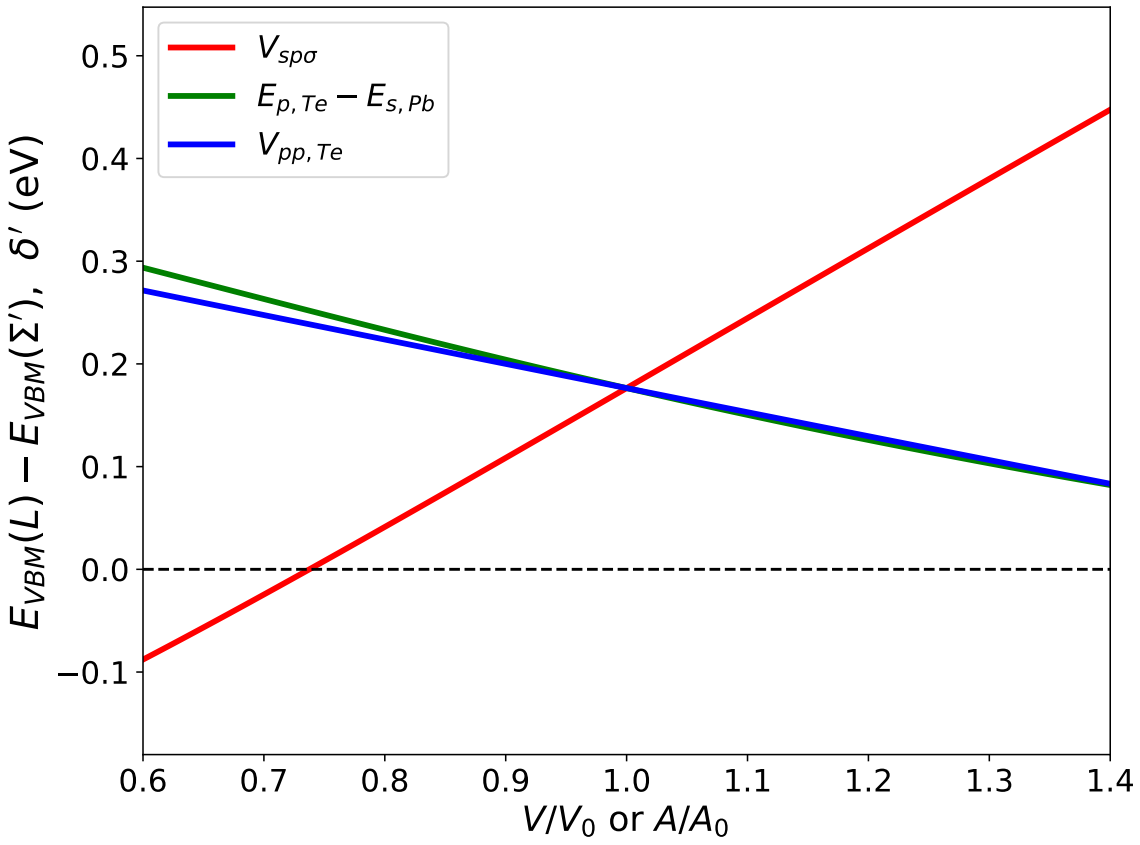

Figure 5: Analytical trends in $\delta' = E_{VBM}(\mathrm{L}) - E_{VBM}(\Sigma')$, a proxy for VB convergence, as a function of $V_{sp\sigma}$, A, and $V_{pp,Te}$ (normalized to their initial values). The bands become more converged (δ decreases) as the splitting between the Pb-s and Te-p on-site energies ($2A$) and the interaction strength of the Te-p orbitals ($V_{pp,Te}$) increase and as the interaction strength of the Pb-s and Te–p orbitals ($V_{sp\sigma}$) decreases. The VB convergence of PbTe can be tailored by engineering the orbital interactions towards $\delta' = 0$.

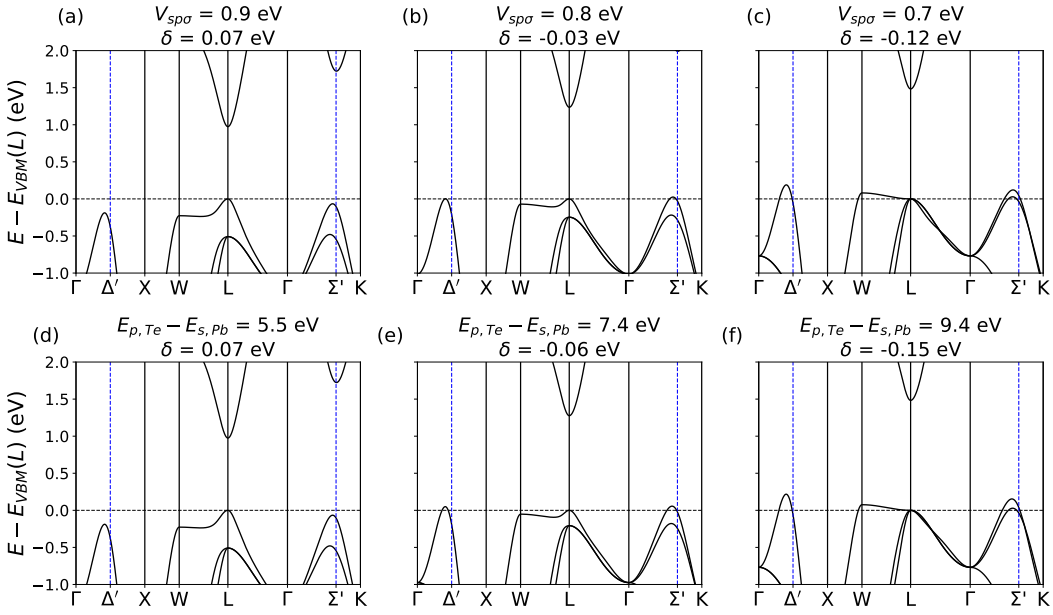

Figure 6: Evolution of TB bands for PbTe calculated (without SOC) as the overlap parameter describing the interaction between the Pb-s and Te-p states, $V_{sp\sigma}$, and the energy splitting between these two states varies. As $V_{sp\sigma}$ decreases from (a)-(c), the CBM at L increases in energy relative to the VBM at L, the Σ, Δ, and W VBMs increases in energy relative to the L VBM. The three L VBs also converge. The same trend is seen in (d)-(f) as the Pb-s state is decreases away from the Te-p on-site energy, increasing A. Note that the δ values are calculated based on the calculated maximum along Σ and not the exact Σ'-point.

In these thought experiments, we vary individual TB parameters at a time, while keeping the others fixed. In reality, these parameters are coupled in such a way that one parameter would not change in isolation. For instance, increasing the lattice parameter via strain or temperature would decrease all of the overlap parameters by a certain factor due to the increase in interatomic distance. While it is not realistic to change the strength of only a single orbital interaction in a real material, this novel approach allows us to gain a more direct understanding of the mechanism behind the evolution of a band structure upon the modification of the material (via alloying, doping, strain, temperature effects, etc) in terms of recognizable atomic orbitals.

The progression of the calculated E vs. k relationship for PbTe as the $V_{sp\sigma}$ parameter is varied from its initial value to $V^*_{sp\sigma}$ (moving down the red line in Fig. 5) can be seen in Fig. 6a-c. In Fig. 6d-f, we see the evolution of the band structure as Pb-s decreases to increase $A = \frac{1}{2}(E_{p,Te} - E_{s,Pb})$ (green line in Fig. 5) to its critical value of $A^* = 4.7$ eV, or $E_{p,Te} - E_{s,Pb} = 9.4$ eV. We see virtually identical trends in the VB behavior from a-c as from d-f, showing that the method of tailoring the VBs does not affect the topology of the final state. Because the anion s–p interactions are not considered in the evaluation of $V^*_{sp\sigma}$ and A^*, the convergence condition leads to a negative value of the calculated δ when the approximation, $\delta' = 0$. A negative value of δ simply means that the VBM at Σ^* is higher than the L VBM. We see simultaneous convergence of the L and Σ band extrema and of the three L valence bands. Additionally, the maxima of the Δ and W VBs increase in energy relative to the L VBM, such that they also converge with the L and Σ bands. This is extremely promising behavior because it suggests the possibility of achieving even higher valley degeneracy than expected from only the convergence of the L and Σ VBMs.

Furthermore, the bandgap energy, E_g, decreases as $V_{sp\sigma}$ increases, which is evident from the fact that the CBM at L increases in energy relative to the position of the VBM at L as $V_{sp\sigma}$ decreases. As the strength of this interaction increases, the energy VBM at L increases, while the CBM remains the same. More details on the TB analytical expression for E_g can be found in Appendix C. The increased convergence of the L, Σ, Δ, and W bands with the reduction of $V_{sp\sigma}$ can be attributed to the fact that the energy of the L VBM (Eq. 2) has a greater dependence on $V_{sp\sigma}$ than the energy of the Σ, Δ, and W VBMs do (Eqs. 5, 10, and 13). Therefore, as $V_{sp\sigma}$ decreases, the energies of the L, W, Δ, and Σ VBMs all decrease, but the energy of the L band decreases the most rapidly.

The thought-experiment results from varying $V_{sp\sigma}$ and A with SOC interactions considered and from changing the anion-site parameters ($V_{sp\sigma,Te}$, $E_{p,Te} - E_{s,Te}$, and $V_{pp,Te}$) can be found in the Supporting Information (Figs. S1-S4). The Σ and Δ maxima increase in energy relative to the L band as $V_{sp\sigma,Te}$ increases (Fig. S2), the anion s–p splitting ($E_{p,Te} - E_{s,Te}$) decreases (Fig. S3), and $V_{pp,Te}$ increases (Fig. S4). As expected, the relative energy of the W band is unchanged upon varying $V_{sp\sigma,Te}$ and $E_{p,Te} - E_{s,Te}$, as it has no dependence on the anion s–p interactions. In general, for interactions between an anion state and cation state, the effect of increasing the interaction parameter is qualitatively analogous to decreasing the on-site energy difference between the interacting orbitals. This yields two separate routes to tuning s-p coupling. Furthermore, a

greater value of $V_{pp,Te}$ increases the energy of the W, Σ, and Δ bands relative to the L band, as expected.

The trends in the TB description of the PbTe VBs, give us several potential routes for increasing convergence: decrease the strength of (filled) cation-s/anion-p interactions, increase the strength of the anion-p/anion-p interactions, alloy with a cation that has cation-s state lower than Pb-s (increase A), increase the strength of the anion s–p interactions, and decrease the s–p splitting of the anion on-site energies. All of the strategies given here assume that we are starting with $E_{VBM}(\mathrm{L}) > E_{VBM}(\Sigma^*)$, but the opposite statements are true when $E_{VBM}(\mathrm{L}) < E_{VBM}(\Sigma^*)$.

Decreasing the strength of the filled cation-s/anion-p interactions can be achieved by increasing the lattice parameter because of the $1/d^2$-dependence of the TB overlap parameters. Although lattice expansion would decrease $V_{sp\sigma}$, $V_{pp,Te}$, and $V_{sp\sigma,Te}$, the effect on convergence is strongest upon varying $V_{sp\sigma}$. This is consistent the increase in the L band relative to Σ band as temperature increases, found experimentally and from first-principles calculations.[4,41] We can also tune convergence by alloying with a defect that would increase the lattice parameter. SnTe and PbSe both have a smaller lattice parameter and exhibit a greater separation of the Σ and L bands at a given temperature.[4,63] However, it is worth noting that the trends in convergence with respect to modifying the anion-p/anion-p and anion-s/anion-p interactions are not consistent with observed experimental trends in convergence with respect to temperature. This contradiction tells us that the increase in convergence of the L and Σ VB extrema upon an increase in temperature or increase in lattice parameter is due to the cation-s/anion-p interaction. Therefore, we do not consider in detail the strategies involving increasing the strength of the anion-s/anion-p interaction or the anion-p/anion-p interactions in this study. That being said, we can focus on tuning the anion s-p splitting as a means to modify the anion-s/anion-p interaction. Because convergence is favored with a smaller amount of s–p splitting in the anion states, Te is a better choice than Se when the L band is higher than the Σ band because the s–p splitting energy decreases from Se to Te[60]. At higher temperatures ($T > 700$ K) where the Σ band is higher, alloying with PbTe with Se would be beneficial. This is consistent with the experimental finding that shows alloying PbTe with Se increases the L VB relative to the Σ band.[4]

3.4 Influence of Cation-Site Defects on VB Convergence

The results of the previous section help to explain experimental results that show that cation doping can enhance VB convergence and suggest that there are routes to enhance this even further.[21,33,35,36,47–49,69] One technique for doing so involves alloying to introduce cation-s states below the Pb-s states (at the expense of Pb-s states). This would be equivalent to moving down (left to right) the green line in Fig. 5 (increasing A). In order to achieve this, it is necessary to alloy the Pb site with an element that exhibits greater s–p splitting, such as Ge.[60] Therefore, we think this explains why promising materials have been found in PbTe–GeTe alloys as a means to engineer more highly converged VBs. GeTe has attracted much attention as a high-performing thermoelectric ma-

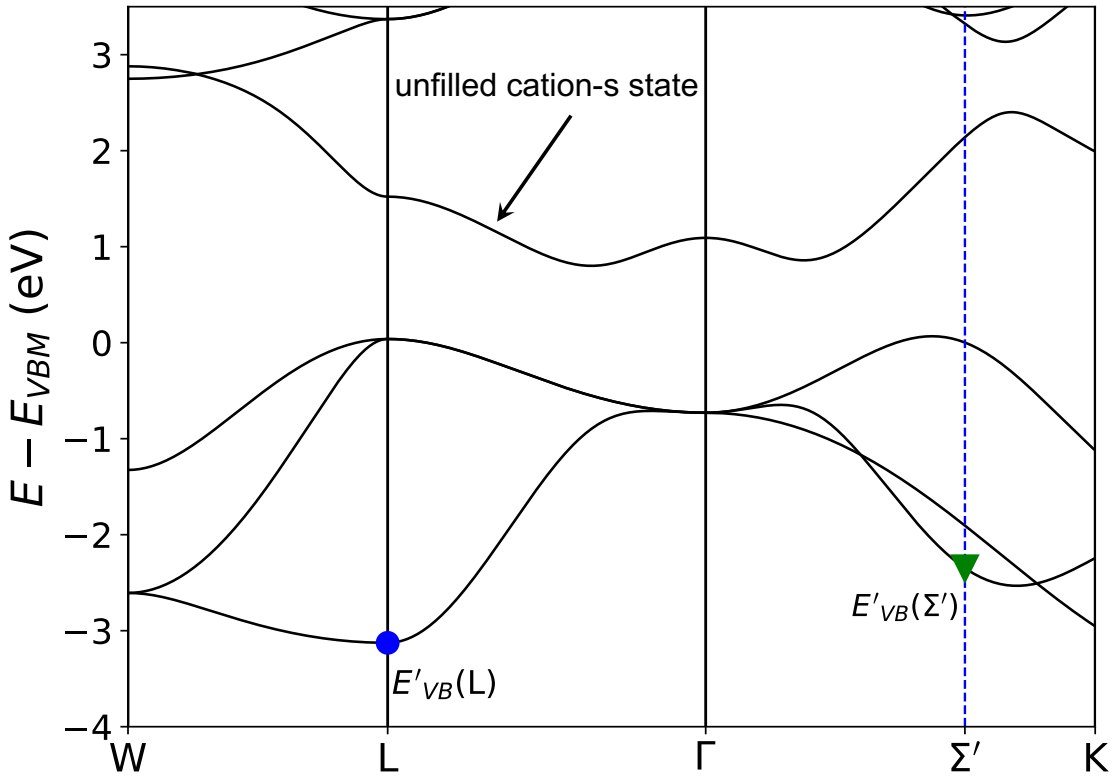

Figure 7: TB electron dispersion of a model rock salt structure where there is an unfilled cation-s above the filled anion-p states. The energies of the states that correspond to the maxima of the L and Σ bands in PbTe are labeled with a blue circle at E'_{VB}(L) and green inverted triangle at $E'_{VB}(\Sigma')$, respectively. Replacing the filled Pb-s states with unfilled cation-s states moves these energies down such that they are local minimums instead of local maxima like they are in PbTe.

terial,[70–74] so it is worth considering the role of the large s–p splitting in its performance. On the other hand, Tl would introduce a cation-6s orbital with an on-site energy higher in energy relative to the Pb-6s orbital but still below the Te-5p states.[60] This type of impurity is predicted to reduce the convergence of the VBs by increasing the L VBM relative to the Σ, Δ, and W VBMs. However, Tl is known to be a very effective *p*-type dopant that actually enhances the thermoelectric power of PbTe:Tl relative to that of pristine PbTe.[40,75–77] This divergence from the predicted behavior here is due to the fact that Tl is a resonant impurity, as the Tl-6s states overlap with the Te-5p states, and resonant impurities are known to substantially increase thermoelectric performance by increasing the DOS near the band edge.[75,77–82]

A potentially powerful route to engineering highly converged VBs that exhibit the 2D topology is to alloy in such a way to introduce unfilled cation-s (s^0) states higher in energy than the anion-p states. This strategy is consistent with the experimental trends seen upon the addition of cation-site dopants (Cd, Hg, Mn Na, Sr, and Mg).[21,33,35,36,47–49,69,83] When these cation-site dopants are substituted on the Pb-site of PbTe, they introduce cation-s states above the Te-p-dominated VBs at the expense of the Pb-s states located below[60].

The TB model for a generic rock salt structure can be modified to help understand the effect of defect-s states on the electron dispersion. We use this as a thought experiment to understand the TB eigenstates in the MTe end-member (M = Mg, Mn, Cd, Na, Sr or Hg) in PbTe-MTe alloys. Fig. 7 shows the electron dispersion corresponding to a rock salt structure where there is an unfilled cation-s state ∼1.6 eV above the anion-p states. The splitting between the cation-p and anion-p states, the anion p–p interactions, and the strength of $V_{sp\sigma}$ all correspond to the values used to approximate PbTe electronic structure shown in Fig. 3. We choose 1.6 eV for the difference between the anion-p and filled cation-s state because this is approximately the difference between the on-site energy differences of Te-p and Cd-s states.[60] The eigenstates that correspond to the VBMs of the L and Σ in PbTe are labeled in Fig. 7 with a blue circle and green inverted triangle, respectively. It is important to note that when the (unfilled) cation-s states are above the Te-p states, the eigenstates that were the VBMs in PbTe are now the lower of the three Te-p states at both L and Σ′.

Consider the cation defect, M, with unfilled s^0 states. When the cation M-s states are entirely above the anion-p states, the energy corresponding to the VBM eigenstates at the L– and Σ–points must be modified from those given in Eqs. 2 and 5. When the anion s–p interactions are ignored, these eigenstates, denoted $E'_{VB}(\mathrm{L})$ and $E'_{VB}(\Sigma')$, are given by Eqs. 22 and 23, respectively. In these expression, $V'_{sp\sigma}$ denotes the TB overlap parameter between the defect cation-s (M-s) state and the Te-p states. The expressions for $E'_{p,Te}(\mathrm{L})$ and $E'_{p,Te}(\Sigma')$ are the same as those given in Eqs. 3 and 6, respectively.

$$E'_{VB}(\mathrm{L}) = \frac{1}{2}\left(E_{s,M} + E'_{p,Te}(\mathrm{L})\right) - \frac{1}{2}\sqrt{\left(E_{s,M} - E'_{p,Te}(\mathrm{L})\right)^2 + 48V'^2_{sp\sigma}} \tag{22}$$

$$E'_{VB}(\Sigma') = \frac{1}{2}\left(E_{s,M} + E'_{p,Te}(\Sigma')\right) - \frac{1}{2}\sqrt{\left(E_{s,M} - E'_{p,Te}(\Sigma')\right)^2 + 32V'^2_{sp\sigma}} \quad (23)$$

The only difference between the solutions for the case where the cation-s states are above the anion-p states and where the cation-s states are below the anion-p states (like in PbTe) is that there is a minus (-) sign in front of the radical in the former case and a plus (+) sign in the latter case. In both cases, there is a repulsive interaction between the Te-p and cation-s states at the L-point and at the Σ'-point that is stronger at the L-point. However, when the cation-s state is below the Te-p states, it pushes the energy of the Te-p state up, but when it is below the Te-p state, it pushes it down, with the force at L being stronger than it is at Σ'. The unfilled defect-s state will also push the W and Δ maxima down, but to a lesser extent than at L .

When these defect M-s states are incorporated into PbTe the repulsive interaction between the unfilled defect-s states with the filled Te-p states partially counteracts the repulsive interaction between the filled Pb-s states and Te-p states. In other words, the presence of these cation-s defect states effectively weakens the repulsive interaction between the Pb-s and Te-p states, $V_{sp\sigma}$. As shown in analytically in Fig. 5 and numerically in Fig. 6, weakening $V_{sp\sigma}$ decreases δ, thus increasing convergence, given that the L band is higher in energy than the Σ band. Furthermore, the effective weakening of $V_{sp\sigma}$ is expected to increase the bandgap energy (see Appendix C). These effects are consistent with what is observed experimentally upon the addition of Mg, Cd, Mn, Sr, Na, and Hg in PbTe; the energy of the Σ VB increases relative to the energy of the L band, and E_g increases.[35,36,47–49,69]

3.5 Low-Dimensional Behavior of Converged PbTe Electronic Structure

Low-dimensional materials have been studied as a means to engineer and enhance thermoelectric transport properties.[5,22,24–26,30,40,84] Typically, low-dimensional electronic structures are expected in nano-structured materials that physically confine the electrons, such as thin-film with thickness on the nano-scale, nanowires, and quantum dots.[5,25,26,84] While improvements can be seen in low-dimensional materials with a one sub-band model, when all degenerate bands and sub-bands are included in the transport of the bulk system, the quantum confinement in low-dimensional materials is detrimental to thermoelectric performance, as it breaks band degeneracy.[28,29] However, properties of low-dimensional electronic structures also exist in bulk 3D materials, and these materials do not exhibit degeneracy-breaking quantum confinement.[22,24,30,40,74,85] For instance, Dylla *et al.* found that $SrTiO_3$ has a Fermi surface that can be described as three orthogonal 2D cylindrical Fermi surfaces, and therefore; it exhibits some transport properties that would be expected from a 2D material despite the sample being in its bulk 3D form.[30] Enhanced thermoelectric performance has been predicted for a 3D bulk materials with a 2D Fermi surfaces.[22,24] Note that when we refer to 1D, 2D, and 3D Fermi surfaces, we are not describing the dimensionality of the Fermi surface geometry itself, but rather to the dimensionality of the density of electronic states described by

that Fermi surface. That is, for a 1D or 2D topology, the Fermi surface expands with energy in only one or two dimensions giving a DOS like that of a true 1D or 2D system.

Here, we compare two "states" for the VB structure based on the relative strength of the cation-s/anion-p interaction: converged ($V_{sp\sigma} = 0.75$ eV) and "not converged" ($V_{sp\sigma} = 0.9$ eV). The terms "converged" and "not converged" are simply relative descriptors of the VB structure. As discussed in the prior section, multiple parameters can be adjusted to tune convergence, but for simplicity, we limit our study here to a variation in $V_{sp\sigma}$. When the PbTe VBs are not in a highly converged state, the Fermi surface just below the VB edge would be described by ellipsoidal pockets (4 total) around L (Fig. 1a).[4,40,74] As the VBs become more converged ($V_{sp\sigma} = 0.75$ without SOC), the VB edge in the electronic dispersion becomes nearly flat along the W–L–Σ^*–Δ^* directions (Fig. 8a). Recall that Σ^* and Δ^* are the true, calculated values for the local maxima along those directions and change depending on the parameters used in the calculations (and whether or not SOC is included).

This flat band dispersion results in the Fermi surface fairly close to the band edge exhibiting unique 1D character despite the material itself being in its bulk 3D form. As seen in Fig. 8c, the VB Fermi surface (calculated 0.10 eV below the L VBM) can be described as a set of orthogonal sheets of a finite width that contain the L–, Σ^*–, Δ^*–, and W– points in the BZ. There are two sheets along each of the three Cartesian directions. Unlike a traditional 1D material, such as a nanowire, net electronic transport in this system occurs identically along all three Cartesian directions, but is restricted to a single direction on a given sheet of the Fermi surface. In this way, it can be thought of as the electronic structure of three orthogonal 1D systems. For the component of the conductivity along the x-direction, only the sheets oriented in the $y - z$ plane would contribute to the transport, with analogous behavior for the y- and z- directions.

Assuming parabolic bands characterized by a unique effective mass in each direction, the 3D electronic structure of a material can be described by the dispersion relationship shown in Eq. 24, where m_x m_y, and m_z are the effective masses along each of the three Cartesian directions.[5,30,86] The effective mass is inversely proportional to the curvature of the dispersion relationship in its respective direction. That is, $m_i = \hbar^2(d^2E/dk_i^2)^{-1}$.[4,86,87]

$$E(k_x, k_y, k_z) = \frac{\hbar^2 k_x^2}{2m_x} + \frac{\hbar^2 k_y^2}{2m_y} + \frac{\hbar^2 k_z^2}{2m_z} \tag{24}$$

For a given sheet in the converged PbTe VB Fermi surface, the curvature is zero in two of the three directions. The effective mass in the two flat directions approaches infinity.[30] The velocity of the charge carrier in a given direction is related to the partial derivative of the dispersion relationship.[30,86]

$$v_i(\mathbf{k}) = \frac{1}{\hbar}\frac{\partial E(\mathbf{k})}{\partial k_i} = \frac{\hbar k_i}{m_i} \tag{25}$$

In Equation 25, v_i is the carrier velocity along the i–direction, where $i = x, y$, or z. The velocity in a given direction is inversely proportional to the respective effective mass. Therefore, when there is virtually zero dispersion in a given direction (flat band), then the effective mass in that direction approaches infinity, and the velocity approaches zero. Consequently, the carrier transport is effectively zero in that direction and limited to the other direction(s).

When studying PbTe, it is important to consider SOC effects to gain a more accurate representation of the electronic structure.[88–92] While the analytical solutions are not found with SOC interactions considered, the TB bands were calculated with SOC using the value of $V_{sp\sigma} = 0.75$ and a Te SOC parameter of 0.3 eV (Fig. 8b). While the three VBs at L, the VB extrema at W and at Δ^*, and the two highest VBs along Σ are not as highly converged upon the addition of SOC, the maxima of the L and Σ VBs are still nearly converged with each other. Therefore, the convergence condition derived for the L and Σ VBs still holds when SOC is included. The SOC interactions reintroduce curvature in the VB edge between L and W and between Σ^* and Δ^* in the highly converged case, as seen in 8b. As a result, the effective mass near the band edge is finite along two of the three directions, so the Fermi surface 0.10 eV below the L VBM exhibits a 2D instead of a 1D topology. This analysis introduces an additional design strategy: engineering an alloy that weakens the SOC interactions relative to pure PbTe.

The Fermi surface structure we find after introducing SOC resembles the 2D Fermi surface of lead chalcogenides described by Parker and Singh.[24,40] We do not have to go so deep into the VB edge (note that the "depth" is somewhat arbitrary, as this is a model system) to reach this 2D topology as we did to reach the 1D topology shown in 8c; the 2D topology is obtained in the converged bands with SOC only 0.05 eV below the L VBM. The 2D Fermi surface can be described as 12 curved tubes that contain the L-point and Σ maximum in the BZ (Fig. 8d). Later, we approximate these tubes as cylinders to model thermoelectric transport properties via Boltzmann transport model.

Topological transitions in the non-converged bands to lower-dimensional 2D or 1D Fermi surfaces from 3D or 2D Fermi surfaces, respectively, can be achieved by moving the Fermi energy farther below the VB edge. For instance, we can obtain a 2D Fermi surface 0.14 eV below the Fermi energy when $V_{sp\sigma} = 0.9eV$ (not converged), and SOC is included, as seen in Fig. 8e. Additionally, if the Fermi surface in Fig. 8d is expanded to ~ 0.25 eV below the L VBM, then then the cylinders grow into the sheets seen in the highly converged electron bands without SOC (Fig. 8f), as the VB edge is mostly flat along W–L–Σ^*–Δ^* at this energy below the band edge.

In summary, convergence of the L and Σ VBMs alone leads to a 2D Fermi surface topology, and the added convergence of the Δ and W band extrema promotes the 1D topology. In practice, the 2D topology can be achieved mainly by alloying the cation-site with an element that introduces unfilled cation-s states above the VB edge. A secondary approach would involve substituting Pb sites with Ge, which has a greater s-p splitting. Finally, by alloying PbTe to promote convergence of the L, Σ, W, and Δ bands we can reduce the carrier concentration required to achieve the lower-dimensional

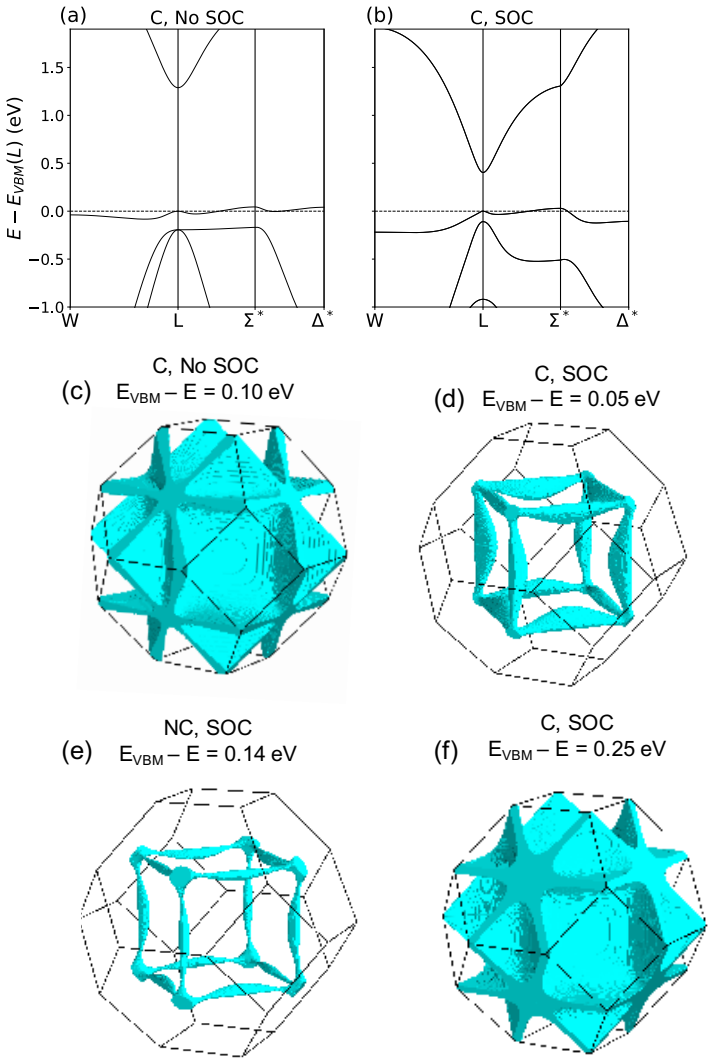

Figure 8: TB electron bands and valence band Fermi surfaces for variations of a PbTe tight-binding model. Σ^* and Δ^* are the true maxima along Σ and Δ. (a) When SOC is not included, the top of the highly converged VB edge is nearly flat along W–L–Σ^*–Δ^*, (b) but when SOC is introduced, curvature is reintroduced along L–W and Σ^*–Δ^*. (c) The Fermi surface 0.10 eV below the L VBM for the highly converged PbTe electronic structure without SOC resembles a set of 6 orthogonal sheets. (d) When SOC is included, the Fermi surface 0.05 eV below the L maximum forms 12 tubes. (e) The thread– or tube–like Fermi surface is found 0.14 eV below the L-point band edge for a non-converged VB edge with SOC. (f) For the highly converged case with SOC, the VBs form sheets 0.25 eV below the L VBM. For (d)-(f) we use C (converged) to denote the highly converged case, where $V_{sp\sigma} = V^*_{sp\sigma} = 0.75$ eV, and NC (not converged) when the original value of $V_{sp\sigma} = 0.9eV$ is used.

Fermi surface topologies. SOC interactions appear to break the high degeneracy required for the 1D topology in favor of the 2D topology. Therefore, the 1D topology could be achieved in a real material by substituting the Te site for S or Se, which have weaker SOC interactions, with S having the weakest.[60,79,89] However, because substituting S or Se for Te on the anion-site would decrease the lattice parameter, thus decreasing convergence of the L, Σ, Δ, and W VB extrema, it is necessary that this is compensated for via the incorporation of the appropriate cation dopants to counteract the effect of reducing the lattice parameter.

3.6 Transport Model for Low-Dimensional Electron Bands

To understand the effect of the low dimensional electron bands on the thermoelectric transport, we use the Boltzmann transport equation (BTE) and compare the computed properties to that of a 3D system.[9,10,12,15,86,87,93–95] We assume electron-phonon scattering dominates where the scattering rate is proportional to the density of electron states, as it is in deformation potential and phonon scattering. It has been shown that phonon, or deformation potential, scattering provides a good description of transport in lead chalcogenides.[18] For the 1D case, we assume a Fermi surface described by 6 sheets (two perpendicular to each Cartesian direction) and a square face with side lengths $l_{1D} = 2\sqrt{2}\pi/a$ where a is the lattice parameter (Fig. 1d). The 2D Fermi surface is approximated by 12 cylinders (4 parallel to each Cartesian direction) with length $l_{2D} = 2\pi/a$ (Fig. 1c).[24] Lastly, the 3D model is described by 4 spheres at L (8 half-spheres) (Fig. 1a).

The dispersion relationship defining the idealized 2D bands is described by Eq. 26, where $i, j = x, y,$ or z, but $i \neq j$.

$$E(k_x, k_y, k_z) = \frac{\hbar^2 k_i^2}{2m_i} + \frac{\hbar^2 k_j^2}{2m_j} \tag{26}$$

Along each tube, the effective mass is infinite along the direction parallel to its length, restricting electronic transport to the other two orthogonal directions. That is, for a cylinder oriented along the z-axis in the BZ, transport would be limited to the x- and y- directions due to infinite effective mass (zero curvature) along the the z-direction.

For the 1D sheet topology, we have the following dispersion:

$$E(k_x, k_y, k_z) = \frac{\hbar^2 k_i^2}{2m_i} \tag{27}$$

In this case, transport is limited to only the i direction, as carrier velocity would be virtually zero along the other two directions.

We provide the expressions for the scattering time, τ, Seebeck coefficient, S, quality factor, B, Lorenz factor L, figure of merit, zT, and DOS, $g(\varepsilon)$, for 1D, 2D, and 3D PbTe bands in Appendix B. Because we are using $\tau \propto 1/g$ the expression for S, L, and zT are identical for 1D, 2D, and 3D

in terms of B and the reduced Fermi Level, η, where $\eta = E_F/k_BT$, and E_F is the Fermi energy. They are given in Eqs. 28-30.

$$S(\eta) = \left(\frac{k_B}{e}\right)\left[\frac{2F_1(\eta)}{F_0(\eta)} - \eta\right] \tag{28}$$

$$L(\eta) = \left(\frac{k_B}{e}\right)^2\left[\frac{3F_2(\eta)F_0(\eta) - 4F_1^2(\eta)}{F_0^2(\eta)}\right] \tag{29}$$

$$zT(\eta, B) = \frac{S^2(\eta)}{\frac{(k_B/e)^2}{BF_0(\eta)} + L(\eta)} \tag{30}$$

$F_i(\eta)$ is the Fermi-Dirac integral, which is defined in Eq. 31.

$$F_i(\eta) = \int_0^\infty \frac{\varepsilon^i d\varepsilon}{1 + e^{\varepsilon - \eta}} \tag{31}$$

Although S is the same for all three dimensions for a given value of η, the reduced chemical potential is a function of the hole concentration, p, which is given by $p = \int_0^\infty g(E)f(E-\mu)dE$, where $f(E-\mu)$ is the Fermi-Dirac distribution. Because the DOS is different for each dimension, the relationship between p and η changes with dimensionality, as seen in Eqs. 32-34, where p_{1D}, p_{2D}, p_{3D} represent the number of holes per unit volume of the material corresponding to the idealized 1D, 2D, and 3D Fermi surface cases for PbTe, respectively. Note that in these expressions, we define the hole concentration in terms of the band effective mass, m_b^* (band curvature mass along the dispersive direction) instead of an equivalent DOS effective mass, m_{DOS}^*, which we shall define later.

$$p_{1D} = \frac{12(2m_b^* k_B T)^{1/2}}{a^2 \pi \hbar} F_{-\frac{1}{2}}(\eta) \tag{32}$$

$$p_{2D} = \frac{12 m_b^* k_B T}{a \pi \hbar^2} F_0(\eta) \tag{33}$$

$$p_{3D} = \frac{2(2m_b^* k_B T)^{3/2}}{\pi^2 \hbar^3} F_{\frac{1}{2}}(\eta) \tag{34}$$

Using Eqs. 32-34 and Eq. 28, we can calculate the Pisarenko relationship at 300K (S vs. p) for each dimension as seen in Fig. 9a. The lattice parameter is taken to be $a = 6.46$ Å, and the band effective mass is taken to be $m_b^* = 0.2m_e$.[24] For a given η, the Seebeck coefficient increases as the dimensionality of the bands is reduced. This increase in thermopower as the band dimensionality progresses from 3D to 1D is attributed to the higher hole concentration for a given η due to the general increase in Fermi surface area from the 3D to 1D case. The zT vs. p curve

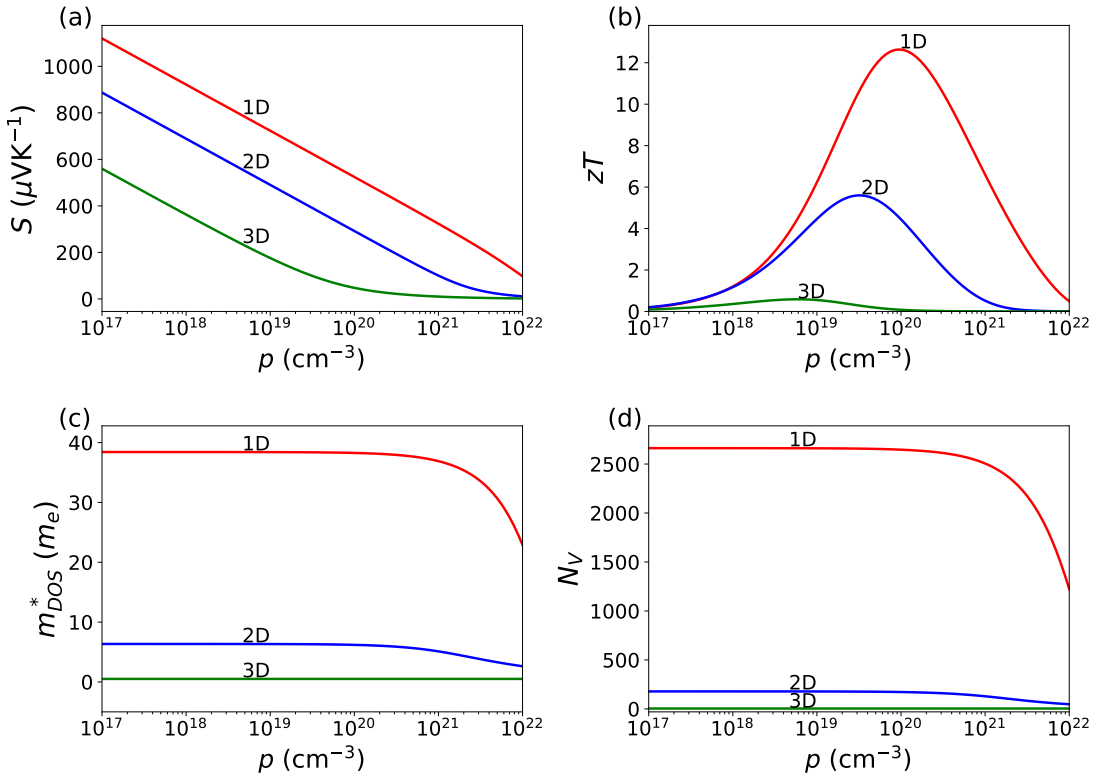

Figure 9: Transport model analysis for 1D, 2D and 3D Fermi surface topologies in PbTe assuming phonon scattering, a lattice thermal conductivity of $\kappa_L = 1.5$ $\mathrm{Wm^{-1}K^{-1}}$, and mobility parameter of $\mu_0 = 1200$ $\mathrm{cm^2V^{-1}s^{-1}}$. (a) Pisarenko plots ($S$ vs. p) for PbTe with 1D, 2D and 3D Fermi surfaces. (b) zT vs. p curves for the 1D, 2D, and 3D models. The 3D model yields a peak $zT \sim 0.6$, the 2D model gives a peak $zT \sim 6$, and the 1D model predicts a peak $zT \sim 13$. (c) The effective (3D) m^*_{DOS} increases from $m^*_{DOS} = 0.5m_e$ for the 3D topology, to $m^*_{DOS} \sim 6m_e$ for 2D, and to $m^*_{DOS} \sim 40m_e$ predicted for fully converged, 1D PbTe. (d) The maximum effective valley degeneracy, N_V, increases from $N_V = 4$ for the 3D model to $N_V \sim 180$ for the 2D model and to $N_V \sim 2700$ for the 1D model.

at 300K is then calculated based on Eq. 30, assuming a constant lattice thermal conductivity of $\kappa_L = 1.5$ $\mathrm{Wm^{-1}K^{-1}}$ [16] and a constant mobility parameter, μ_0, of 1200 $\mathrm{cm^2V^{-1}s^{-1}}$.[39] Note that these are approximate values assumed for the sake of comparing the thermoelectric performance from the different Fermi surface topologies. In reality, these value depend on temperature and carrier concentration. The value of μ_0, was estimated based Hall effect on data from Crocker and Rogers.[39] It is found that the maximum predicted zT is greatest for the 1D Fermi surface, followed by the 2D and then the 3D topology (Fig. 9b). We predict a peak $zT \sim 0.6$ at $p \sim 6 \times 10^{18}$ $\mathrm{cm^{-3}}$ for the 3D model, $zT \sim 6$ at $p \sim 3 \times 10^{19}$ $\mathrm{cm^{-3}}$ for the 2D model, and $zT \sim 13$ at $p \sim 1 \times 10^{20}$ $\mathrm{cm^{-3}}$ for the 1D case.

We apply the effective mass model for the 3D case to the Pisarenko calculations for the 1D and 2D models to determine a 3D equivalent DOS effective mass ($m^*_{DOS} = m^*_b N_V^{2/3}$) for each value of p (Fig. 9c) and then calculate an effective valley degeneracy[46] at each carrier concentration (Fig. 9d). To perform this analysis, the equation for the carrier concentration in terms of the density of states mass, m^*_{DOS}, corresponding to the 3D model is needed. We assume a valley degeneracy of $N_V = 4$ for the 3D model with carrier pockets at L, so we can simply rewrite Eq. 34 as shown below.

$$p_{3D} = \frac{(2m^*_{DOS}k_BT)^{3/2}}{2\pi^2\hbar^3}F_{\frac{1}{2}}(\eta) \tag{35}$$

Applying Eqs. 35 and 28 to the calculated Pisarenko curves in Fig. 9a, we can calculate m^*_{DOS}, and for each value of m^*_{DOS}, we determine an effective N_V through the expression $N_V = (m^*_{DOS}/m^*_b)^{3/2}$. For this analysis, we treat all of the S vs. p data as if it comes from 3D parabolic bands, regardless of the true dimensionality of the Fermi surface from which it comes. m^*_{DOS} and N_V are both constant for the 3D model with respect to p, but for the 1D and 2D models, they are a function of carrier concentration. They initially plateau then start decreasing between $p \sim 10^{21} - 10^{22}\mathrm{cm^{-3}}$. For the 3D model, we obtain $m^*_{DOS} = 0.5m_e$, corresponding to $N_V = 4$. At the value p corresponding to the peak zT, we calculate $m^*_{DOS} \sim 6m_e$ and $N_V \sim 180$ for the 2D case and $m^*_{DOS} \sim 40m_e$ and $N_V \sim 2600$ for the 1D model. Clearly, a the topological transition to lower-dimensional Fermi surface yields a massive increase in transport channels. These values of effective N_V are much greater than what we would expect from simply adding the valley degeneracies of the VB extrema (4(L)+12(Σ)+6(W)+6(Δ) = 28), suggesting that a shift to studying topology changes in the band structure is necessary for predicting transport behavior in highly converged electronic structures.

Because the quality factor is proportional to N_V, if we apply the 3D effective mass model to the 1D and 2D bands, we predict a significantly higher B for the 1D and 2D cases. The quality factor for the 3D PbTe band model used here is constant at $B = 0.2$, but for the 1D and 2D models, the quality factor that corresponds to the 3D model varies as a function of the hole concentration, p. Therefore, we use the values of B corresponding to the maximum predicted zT for comparison purposes. The quality factors at the maximum zT's for the 2D and 1D bands are approximately

$B \sim 9$ and $B \sim 130$, respectively, showing significant gains relative to the 3D bands. It is important to note that the predicted values for N_V, and consequently m^*_{DOS} and B, and zT, represent upper-bounds and most certainly overestimate the true valley degeneracy and thermoelectric performance because of inter-valley scattering and other assumptions made here. These extremely high values predicted for the 1D band topology are purely theoretical but give an idealized electronic structure to strive for and motivates the search for convergence beyond that found in the 2D topology. Even achieving a band structure intermediate between the 2D and 1D cases would vastly improve thermoelectric performance.

4 Conclusion

We present analytical solutions for a TB approximation of the PbTe VB structure to better understand the orbital interactions that lead to higher VB convergence and to changes in the topology of the electronic structure. We use the analytical TB expressions without SOC to determine qualitative trends in VB convergence with respect to orbital interaction strengths and orbital on-site energies ($V_{sp\sigma}$, $V_{pp,Te}$, and $2A = E_{p,Te} - E_{s,Pb}$). There is a critical value for these three parameters where the VB extrema at L and Σ' are approximately converged. When SOC interactions are minimal, the Δ and W bands are also effectively converged with the L and Σ band at this point, resulting in a 1D Fermi surface topology. When SOC is introduced, approaching the same critical value of $V^*_{sp\sigma}$ leads to the convergence of the L and Σ VBs, but the topology of the bands has 2D character, as SOC breaks the convergence with other the VB pockets (W and Δ).

Based on the qualitative trends determined with the TB model, we propose several alloying design strategies based on anion-cation and anion-anion interactions to tailor the valence bands in such that they approach the highly converged 1D topology. The recommended strategies are listed below:

i Introduce unfilled cation-s (s^0) defect states above anion-p states (Cd, Mg, Hg, Mn, Sr, and Na)

ii Increase lattice parameter via alloying or temperature increase

iii Decrease anion s–p splitting

iv Introduce cation-s defect states below Pb-s states (at the expense of Pb-s states)

v Minimize the strength of the (anion) SOC interactions

We apply an effective mass model using the BTE to predict thermoelectric transport values for the 3D, 2D, and 1D bands and predict enhanced thermoelectric performance when the dimensionality of the bands decreases, which occurs as more VB pockets converge. The increase

in predicted thermoelectric performance is understood by applying the 3D effective mass model to the 1D and 2D bands, and we predict substantial gains in thermoelectric performance from a massive increase in the number of transport channels available in 2D and 1D bands. The 1D and 2D transport behavior is analogous to 3D behavior with extremely high valley degeneracy, and therefore a significantly enhanced quality factor and zT. The gains in performance are greater for the 1D bands than the 2D bands, suggesting that engineering or alloying PbTe or other materials to achieve this unique 1D topology could lead to tremendous gains in thermoelectric performance and theoretically lead to $zT > 10$, roughly 20 times larger than the zT we predict for the 3D ellipsoidal Fermi surface topology. While this extremely high zT is only a theoretical prediction for a highly idealized case, it motivates work towards increasing VB convergence beyond that found in the 3D and 2D Fermi surface topologies. By strategically alloying PbTe based on the qualitative trends discussed here, it is possible to tune and reduce the doping concentration needed to achieve these favorable, low-dimensional Fermi surface topologies.

Conflicts of Interest

There are no conflicts to declare.

Acknowledgements

This work was supported by NSF DMREF award # 1729487. The authors also thank Michael Toriyama for his helpful discussion and insights.

Supporting Information

Supporting information is available [insert SI file]

References

[1] L. E. Bell, *Science*, 2008, **321**, 1457–1461.

[2] G. J. Snyder and E. S. Toberer, *Nat. Mater*, 2008, **7**, 105–114.

[3] A. D. LaLonde, Y. Pei, H. Wang and G. Jeffrey Snyder, *Mater. Today*, 2011, **14**, 526 – 532.

[4] Y. Pei, X. Shi, A. Lalonde, H. Wang, L. Chen and G. J. Snyder, *Nature*, 2011, **473**, 66–69.

[5] L. D. Hicks and M. S. Dresselhaus, *Phys. Rev. B*, 1993, **47**, 12727–12731.

[6] A. Zevalkink, D. M. Smiadak, J. L. Blackburn, A. J. Ferguson, M. L. Chabinyc, O. Delaire, J. Wang, K. Kovnir, J. Martin, L. T. Schelhas, T. D. Sparks, S. D. Kang, M. T. Dylla, G. J. Snyder, B. R. Ortiz and E. S. Toberer, *Appl. Phys. Rev.*, 2018, **5**, 021303.

[7] M. G. Kanatzidis, *Chem. Mater.*, 2010, **22**, 648–659.

[8] H. Peng, J. H. Song, M. G. Kanatzidis and A. J. Freeman, *Phys. Rev. B Condens. Matter*, 2011, **84**, 1–13.

[9] S. D. Kang and G. J. Snyder, *arXiv*, 2017, 1–5.

[10] H. Goldsmid, *Introduction to Thermoelectricity*, Springer Berlin Heidelberg, 2009.

[11] A. S. Anke Weidenkaff, Matthias Trottmann, Petr Tomeš, Clemens Suter and A. Veziridis, in *Thermoelectric Nanomaterials: Materials Design and Applications*, 2013, vol. 182, p. 389.

[12] A. May and G. Snyder, in *Introduction to modeling thermoelectric transport at high temperatures*, CRC Press, 2017, pp. 11–1–11–18.

[13] G. Mahan, *Solid State Physics*, Academic Press, 1998, vol. 51, pp. 81 – 157.

[14] H. J. Goldsmid, *Thermoelectric Refrigeration*, Plenum Press, New York, 1964.

[15] S. Dongmin Kang and G. Jeffrey Snyder, *Nat. Mater*, 2017, **16**, 252–257.

[16] Y. Pei, H. Wang and G. J. Snyder, *Adv. Mater.*, 2012, **24**, 6125–6135.

[17] Z. M. Gibbs, F. Ricci, G. Li, H. Zhu, K. Persson, G. Ceder, G. Hautier, A. Jain and G. J. Snyder, *Npj Comput. Mater*, 2017, **3**, 1–6.

[18] H. Wang, Y. Pei, A. D. LaLonde and G. Jeffery Snyder, in *Material Design Considerations Based on Thermoelectric Quality Factor*, ed. K. Koumoto and T. Mori, Springer Berlin Heidelberg, Berlin, Heidelberg, 2013, pp. 3–32.

[19] J. Park, M. Dylla, Y. Xia, M. Wood, G. J. Snyder and A. Jain, *When Band Convergence is Not Beneficial for Thermoelectrics*, 2020.

[20] I. T. Witting, F. Ricci, T. C. Chasapis, G. Hautier and G. J. Snyder, *Research*, 2020, **2020**, 1–15.

[21] Y. Pei, A. D. LaLonde, N. A. Heinz, X. Shi, S. Iwanaga, H. Wang, L. Chen and G. J. Snyder, *Adv. Mater.*, 2011, **23**, 5674–5678.

[22] D. I. Bilc, G. Hautier, D. Waroquiers, G.-M. Rignanese and P. Ghosez, *Phys. Rev. Lett.*, 2015, **114**, 136601.

[23] R. Kim, S. Datta and M. S. Lundstrom, *J. Appl. Phys*, 2009, **105**, 034506.

[24] D. Parker, X. Chen and D. J. Singh, *Phys. Rev. Lett.*, 2013, **110**, 146601.

[25] L. D. Hicks and M. S. Dresselhaus, *Phys. Rev. B*, 1993, **47**, 16631–16634.

[26] M. Dresselhaus, G. Chen, M. Tang, R. Yang, H. Lee, D. Wang, Z. Ren, J.-P. Fleurial and P. Gogna, *Adv. Mater.*, **19**, 1043–1053.

[27] J. P. Heremans, M. S. Dresselhaus, L. E. Bell and D. T. Morelli, *Nat. Nanotechnol*, 2013, **8**, 471 – 473.

[28] J. E. Cornett and O. Rabin, *Appl. Phys. Lett.*, 2011, **98**, 182104.

[29] J. E. Cornett and O. Rabin, *Phys. Rev. B*, 2011, **84**, 205410.

[30] M. T. Dylla, S. D. Kang and G. J. Snyder, *Angew.*, 2019, **58**, 5503–5512.

[31] L. D. Zhao, V. P. Dravid and M. G. Kanatzidis, *Energy Environ. Sci.*, 2014, **7**, 251–268.

[32] L. D. Zhao, H. J. Wu, S. Q. Hao, C. I. Wu, X. Y. Zhou, K. Biswas, J. Q. He, T. P. Hogan, C. Uher, C. Wolverton, V. P. Dravid and M. G. Kanatzidis, *Energy Environ. Sci.*, 2013, **6**, 3346–3355.

[33] Y. Pei, A. Lalonde, S. Iwanaga and G. J. Snyder, *Energy Environ. Sci.*, 2011, **4**, 2085–2089.

[34] Z. M. Gibbs, A. LaLonde and G. J. Snyder, *New J. Phys.*, 2013, **15**, 075020.

[35] Y. Pei, A. D. LaLonde, N. A. Heinz and G. J. Snyder, *Adv. Energy Mater.*, 2012, **2**, 670–675.

[36] Y. Pei, H. Wang, Z. M. Gibbs, A. D. LaLonde and G. J. Snyder, *NPG Asia Materials*, 2012, **4**, e28–e28.

[37] Y. I. Ravich, B. A. Efimova and I. A. Smirnov, in *Semiconducting Lead Chalcogenides*, Springer, Boston, MA, 1970, vol. 5, ch. Band Structure and Scattering Mechanisms (Theory and Conclusions from Experimental Data), pp. 263–322.

[38] H. Sitter, K. Lischka and H. Heinrich, *Phys. Rev. B*, 1977, **16**, 680–687.

[39] A. J. Crocker and L. M. Rogers, *British J. Appl. Phys*, 1967, **18**, 563–573.

[40] D. J. Singh, *Phys. Rev. B*, 2010, **81**, 195217.

[41] J. D. Querales-Flores, J. Cao, S. Fahy and I. Savić, *Phys. Rev. Materials*, 2019, **3**, 055405.

[42] Z. M. Gibbs, H. Kim, H. Wang, R. L. White, F. Drymiotis, M. Kaviany and G. Jeffrey Snyder, *Appl. Phys. Lett.*, 2013, **103**, year.

[43] R. S. Allgaier, *J. Appl. Phys*, 1961, **32**, 2185–2189.

[44] R. Rustom-Dalouche, S. Rolland, R. Granger and C. M. Pelletier, *physica status solidi (b)*, 1985, **129**, 835–842.

[45] R. N. Tauber, A. A. MacHonis and I. B. Cadoff, *J. Appl. Phys*, 1966, **37**, 4855–4860.

[46] Z. M. Gibbs, F. Ricci, G. Li, H. Zhu, K. Persson, G. Ceder, G. Hautier, A. Jain and G. J. Snyder, *Npj Comput. Mater*, 2017, **3**, 8.

[47] P. Jood, J. P. Male, S. Anand, Y. Matsushita, Y. Takagiwa, M. G. Kanatzidis, G. J. Snyder and M. Ohta, *JACS*, 2020, **142**, 15464–15475.

[48] L. M. Rogers and A. J. Crocker, *J. Phys. D Appl. Phys.*, 1971, **4**, 1006–1015.

[49] A. Crocker and L. Rogers, *Journal de Physique Colloques*, 1968, **29**, C4–129–C4–132.

[50] J. Harris and B. Ridley, *J. Phys. Chem. Solids*, 1972, **33**, 1455 – 1464.

[51] A. Banik, U. S. Shenoy, S. Anand, U. V. Waghmare and K. Biswas, *Chemistry of Materials*, 2015, **27**, 581–587.

[52] G. Tan, W. G. Zeier, F. Shi, P. Wang, G. J. Snyder, V. P. Dravid and M. G. Kanatzidis, *Chemistry of Materials*, 2015, **27**, 7801–7811.

[53] G. Tan, F. Shi, S. Hao, H. Chi, L. D. Zhao, C. Uher, C. Wolverton, V. P. Dravid and M. G. Kanatzidis, *JACS*, 2015, **137**, 5100–5112.

[54] Z. Zheng, X. Su, R. Deng, C. Stoumpos, H. Xie, W. Liu, Y. Yan, S. Hao, C. Uher, C. Wolverton, M. G. Kanatzidis and X. Tang, *JACS*.

[55] D. Wu, L.-D. Zhao, S. Hao, Q. Jiang, F. Zheng, J. W. Doak, H. Wu, H. Chi, Y. Gelbstein, C. Uher, C. Wolverton, M. Kanatzidis and J. He, *Journal of the American Chemical Society*, 2014, **136**, 11412–11419.

[56] J. C. Slater and G. F. Koster, *Phys. Rev.*, 1954, **94**, 1498–1524.

[57] W. A. Harrison, *Pure Appl. Chem.*, 1989, **61**, 2161–2169.

[58] R. Hoffmann, *Angew.*, 1987, **26**, 846–878.

[59] S. Froyen and W. Harrison, *Phys. Rev. B*, 1979, **20**, 2420–2422.

[60] W. Harrison, *Electronic Structure and the Properties of Solids: The Physics of the Chemical Bond*, Dover Publications, 2012.

[61] G. Rohrer, *Structure and Bonding in Crystalline Materials*, Cambridge University Press, 2001.

[62] M. K. Brod, M. Y. Toriyama and G. J. Snyder, *Chem. Mater.*, 2020.

[63] W. G. Zeier, A. Zevalkink, Z. M. Gibbs, G. Hautier, M. G. Kanatzidis and G. J. Snyder, *Angew.*, 2016, **55**, 6826–6841.

[64] X. Xu and W. A. Goddard, *J. Chem. Phys.*, 2004, **121**, 4068–4082.

[65] Z. Y. Ye, H. X. Deng, H. Z. Wu, S. S. Li, S. H. Wei and J. W. Luo, *Npj Comput. Mater*, 2015, **1**, 1–6.

[66] S. H. Wei and A. Zunger, *Phys. Rev. B Condens. Matter*, 1997, **55**, 13605–13610.

[67] H. Zhu, W. Sun, R. Armiento, P. Lazic and G. Ceder, *Appl. Phys. Lett.*, 2014, **104**, 082107.

[68] W. Setyawan and S. Curtarolo, *Comput. Mater. Sci.*, 2010, **49**, 299 – 312.

[69] B. J. Sealy and A. J. Crocker, *J. Mater. Sci.*, 1973, **8**, 1731–1736.

[70] J. Li, X. Zhang, X. Wang, Z. Bu, L. Zheng, B. Zhou, F. Xiong, Y. Chen and Y. Pei, *JACS*, 2018, **140**, 16190–16197.

[71] S. Perumal, S. Roychowdhury and K. Biswas, *J. Mater. Chem.*, 2016, **4**, 7520–7536.

[72] M. Hong, Z.-G. Chen, L. Yang, Y.-C. Zou, M. S. Dargusch, H. Wang and J. Zou, *Adv. Mater.*, 2018, **30**, 1705942.

[73] M. Hong, J. Zou and Z.-G. Chen, *Adv. Mater.*, 2019, **31**, 1807071.

[74] X. Chen, D. Parker and D. J. Singh, *Scientific Reports*, 2013, **3**, 3168.

[75] J. P. Heremans, V. Jovovic, E. S. Toberer, A. Saramat, K. Kurosaki, A. Charoenphakdee, S. Yamanaka and G. J. Snyder, *Science*, 2008, **321**, 554–557.

[76] B. Wiendlocha, *Phys. Rev. B*, 2013, **88**, 205205.

[77] C. M. Jaworski, B. Wiendlocha, V. Jovovic and J. P. Heremans, *Energy Environ. Sci.*, 2011, **4**, 4155–4162.

[78] J. P. Heremans, B. Wiendlocha and A. M. Chamoire, *Energy Environ. Sci.*, 2012, **5**, 5510–5530.

[79] Y. I. Ravich, in *Lead Chalcogenides: Physics and Applications*, CRC Press, 2002, ch. Basic Physical Features of the Lead Chalcogenides.

[80] B. Wiendlocha, *Physical Review B - Condensed Matter and Materials Physics*, 2013, **88**, year.

[81] S. Ahmad, K. Hoang and S. D. Mahanti, *Physical Review Letters*, 2006, **96**, 1–4.

[82] S. Nemov and Y. Ravich, *Uspekhi Fizicheskih Nauk*, 1998, **168**, 817.

[83] G. Tan, F. Shi, S. Hao, L.-D. Zhao, H. Chi, X. Zhang, C. Uher, C. Wolverton, V. P. Dravid and M. G. Kanatzidis, *Nature communications*, 2016, **7**, 12167.

[84] Y. M. Lin and S. Dresselhaus, *Physical Review B - Condensed Matter and Materials Physics*, 2003, **68**, 1–14.

[85] H. J. Xiang and D. J. Singh, *Phys. Rev. B*, 2007, **76**, 195111.

[86] N. Ashcroft and N. Mermin, *Solid State Physics*, Saunders College, Philadelphia, 1976.

[87] V. I. Fistul, *Heavily Doped Semiconductors*, Springer US, New York, NY, 1st edn.

[88] M. Lach-Hab, M. Keegan, D. A. Papaconstantopoulos and M. J. Mehl, *J. Phys. Chem. Solids*, 2000, **61**, 1639–1645.

[89] M. Lach-hab, D. A. Papaconstantopoulos and M. J. Mehl, *J. Phys. Chem. Solids*, 2002, **63**, 833–841.

[90] A. Goyal, P. Gorai, E. S. Toberer and V. Stevanović, *Npj Comput. Mater.*, 2017, **3**, 1–9.

[91] J. O. Dimmock and G. B. Wright, *Phys. Rev.*, 1964, **135**, A821–A830.

[92] P. J. Lin and L. Kleinman, *Physical Review*, 1966, **142**, 478–489.

[93] Y. I. Ravich, B. A. Efimova and I. A. Smirnov, in *Semiconducting Lead Chalcogenides*, Springer, Boston, MA, 1970, vol. 5, ch. Thermoelectric and Thermal Properties, pp. 149–220.

[94] J. Ziman, *Electrons and Phonons: The Theory of Transport Phenomena in Solids*, OUP Oxford, 2001.

[95] X. Zhang, Z. Bu, X. Shi, Z. Chen, S. Lin, B. Shan, M. Wood, A. H. Snyder, L. Chen, G. J. Snyder and Y. Pei, *Sci. Adv.*, 2020, **6**, 6–11.

[96] X. Wang, V. Askarpour, J. Maassen and M. Lundstrom, *arXiv*, 2017, 1–21.

[97] K. Hummer, A. Grüneis and G. Kresse, *Phys. Rev. B Condens. Matter*, 2007, **75**, 1–9.

[98] J. M. Skelton, S. C. Parker, A. Togo, I. Tanaka and A. Walsh, *Phys. Rev. B Condens. Matter*, 2014, **89**, 1–10.

[99] A. R. Murphy, F. Murphy-Armando, S. Fahy and I. Savić, *Phys. Rev. B*, 2018, **98**, 085201.

Appendices

A PbTe Tight-Binding Hamiltonian

The analytical TB solutions for rock salt PbTe without SOC were determined by solving for the eigenvalues of the Hamiltonian given in Eq. A1, using the Slater-Koster matrix elements and following the method outlined by Rohrer.[56,61] The Hamiltonian, $\hat{H}$, is an Hermitian matrix, so $H_{ij} = \bar{H}_{ji}$, where $\bar{H}_{ji}$ is the complex-conjugate of H_{ji}. The 8-dimensional TB basis is comprised of Pb-6s, Pb-6p$_x$, Pb-6p$_y$, Pb-6p$_z$, Te-5s, Te-5p$_x$, Te-5p$_y$, Te-5p$_z$ atomic orbitals. Note that when SOC is included the size of the Hamiltonian increases by a factor of four, as the basis becomes 16-dimensional to account for spin-up and spin-down electrons separately.[88,89]

$$\hat{H} = \begin{pmatrix} H_{11} & H_{12} & \cdots & H_{18} \\ H_{21} & H_{22} & \cdots & H_{28} \\ \vdots & \vdots & \ddots & \vdots \\ H_{81} & H_{82} & \cdots & H_{88} \end{pmatrix} \tag{A1}$$

We do not provide the expressions for every Hamiltonian element here, but representative examples of Hamiltonian elements are given below in Eqs. A2-A9. $E_{a,b}$ represents the on-site energy terms, where a denotes the orbital (s or p) and b denotes the element (Pb or Te). The overlap parameters of the form, $V_{\alpha\beta m}$, where α and β represent the two orbitals (s or p) and m represents the type of bonding (σ or π). When there is an element label in the subscript, the overlap parameter represents the interaction between the next-nearest neighbors for that element (Pb or Te). When there is no element referenced in the subscript, then the parameter represents a nearest neighbor interaction between Pb and Te. However, $V_{sp\sigma 1}$ and $V_{sp\sigma 2}$ are used here to distinguish between the two different nearest neighbor s–p interactions. $V_{sp\sigma 1}$ denotes the interaction between the Pb-s and Te-p orbitals, and $V_{sp\sigma 2}$ denotes the interaction parameter between the Te-s and Pb-p orbitals. Note that this is different than the convention used in the main text, where $V_{sp\sigma}$ denotes the Pb-s/Te-p interaction (since we do not reference the Te-s/Pb-p interaction in the main text).

$$\begin{aligned} H_{11} = E_{s,Pb} + 2V_{ss\sigma,Pb}[&\cos(k_x a/2 + k_y/2) + \cos(k_x a/2 - k_y a/2) + \\ &\cos(k_y a/2 + k_z a/2) + \cos(k_y a/2 - k_z a/2) + \\ &\cos(k_x a/2 + k_z a/2) + \cos(k_x a/2 - k_z a/2)] \end{aligned} \tag{A2}$$

$$H_{12} = -\frac{2i}{\sqrt{2}} V_{sp\sigma,Pb}[\sin(k_x a/2 + k_y a/2) + \sin(k_x a/2 - k_y/2) + \sin(k_x a/2 + k_z a/2) + \sin(k_x a/2 - k_z a/2)] \quad \text{(A3)}$$

$$H_{23} = (V_{pp\sigma,Pb} - V_{pp\pi,Pb})[\cos(k_x a/2 + k_y a/2) - \cos(k_x a/2 - k_y a/2)] \quad \text{(A4)}$$

$$H_{15} = 2V_{ss\sigma}[\cos(k_x a/2) + \cos(k_y a/2) + \cos(k_z a/2)] \quad \text{(A5)}$$

$$H_{16} = -2iV_{sp\sigma 1} \sin(k_x a/2) \quad \text{(A6)}$$

$$H_{25} = -2iV_{sp\sigma 2} \sin(k_x a/2) \quad \text{(A7)}$$

$$H_{26} = 2V_{pp\sigma} \cos(k_x a/2) + 2V_{pp\pi}[\cos(k_a y/2) + \cos(k_z a/2)] \quad \text{(A8)}$$

$$H_{77} = E_{p,Te} + (V_{pp\sigma,Te} + V_{pp\pi,Te})[\cos(k_x a/2 + k_y a/2) + \cos(k_x a/2 - k_y a/2) + \cos(k_y a/2 + k_z a/2) + \cos(k_y a/2 - k_z a/2)] + 2V_{pp\pi,Te}[\cos(k_x a/2 + k_z a/2) + \cos(k_x a/2 - k_z a/2)] \quad \text{(A9)}$$

B Transport Model for 1D, 2D, and 3D Bands in Bulk 3D PbTe

We consider an transport model developed using the Boltzmann transport equation (BTE) [9,10,12,15,86,87,93,94] to model thermoelectric transport in PbTe to understand how it changes as the VBs become more highly converged. The 3D Fermi surface pockets have a degeneracy of 4, and the Fermi-surface cylinders for the 2D case have a degeneracy of 12 , radius k, and length $l_{2D} = 2\pi/a$, where a is the lattice parameter. For a cylinder oriented along the z-axis, $k^2 = k_x^2 + k_y^2$, with analogous expressions for all three directions. In PbTe, the 1D Fermi surface can be described as sheets with thickness $2k$, a square cross-section characterized by a side length of $l_{1D} = 2\sqrt{2}\pi/a$, and degeneracy of 6. For a sheet aligned in the $x - y$ plane, $k = k_z$, with analogues in all three directions.

B.1 Density of States (DOS)

The expressions for the PbTe DOS in each dimension, $g_{mD}(\varepsilon)$ $(m = 1, 2, 3)$, where $\varepsilon = E/k_BT$, and E is the energy below the VB edge, are given in Eqs. B1-B3.

$$g_{1D}(\varepsilon) = \frac{12(2m_b^*)^{1/2}}{a^2\pi\hbar}(k_BT)^{-1/2}\varepsilon^{-1/2} \tag{B1}$$

$$g_{2D}(\varepsilon) = \frac{12m_b^*}{a\pi\hbar^2} \tag{B2}$$

$$g_{3D}(\varepsilon) = \frac{2(2m_b^*)^{3/2}}{\pi^2\hbar^3}(k_BT)^{1/2}\varepsilon^{1/2} \tag{B3}$$

The above expressions for the DOS are used to determine the hole concentrations per unit cell in each dimension, as given in Eqs. 32-34 in the main text.

B.2 Electrical Conductivity, σ

In general, the electrical conductivity is given in Eq. B4.[15,24,86]

$$\sigma(T) = \int \frac{e^2}{3}\tau(E)v^2(E)g(E)\left(-\frac{df}{dE}\right)dE \tag{B4}$$

$v(E)$ is the carrier velocity at a given energy and can be broken down into its direction components. In the 1D topology case $v_x^2(E) = 2E/m_I^*$, in 2D $v_x^2(E) = E/m_I^*$, and in 3D $v_x^2(E) = 2E/3m_I^*$, where $v_x(E)$ is the velocity component along the x-direction. For a cubic material, $v_x = v_y = v_z$. The expression for $v(E)$ is the same regardless of the topology because for the 1D case, $v^2(E) = v_x^2(E)$, in 2D $v^2(E) = 2v_x^2(E)$, and in 3D $v^2(E) = 3v_x^2(E)$, yielding $v^2(E) = 2E/m_I^*$ for all three topologies.[15]

In this model, we assume a DOS dependent scattering rate which would come from an energy-independent matrix element in Fermi's golden rule as used in analytic theories of deformation potential or acoustic phonon scattering.[15] The DOS dependence gives an energy-dependent scattering time, τ, given by $\tau = \tau_0\varepsilon^r$, where r depends on the assumptions made in the scattering-time model used. τ_0 is a constant that is given by $\tau_0 = \frac{\mu_0 m_I^*}{e}$, where m_I^* is the intertial effective mass.[6] For the constant scattering time approximation (τ independent of energy), the scattering exponent is given as $r = 0$. In this paper, where we assume acoustic-phonon scattering, the value of r is $-1/2, 0$, or $1/2$ for the 3D, 2D, and 1D cases, respectively. The value of r for acoustic-phonon scattering is chosen such that $\tau \propto 1/g$.

The term $\frac{e^2}{3}\tau(E)v^2(E)g(E)$ in Eq. B4 can be combined to the single term $\sigma(E)$, which is the electrical conductivity transport function.[15] That is, we can write the electrical conductivity as

$\sigma = \int \sigma(E) \left(-\frac{df}{dE}\right) dE$. Furthermore, $\sigma(E)$ can be written in terms of a transport coefficient, σ_{E_0}, through the expression, $\sigma(E) = \sigma_{E_0}\varepsilon^s$, where $s = 1/2 + r, 1 + r$, or $3/2 + r$ for the 1D, 2D, and 3D cases, respectively, and the form of σ_{E_0} varies with the dimensionality of the band, as seen in the following set of equations.

$$\sigma_{E_0,1D} = \frac{8e\left(2m_e k_B T\right)^{1/2}}{a^2 \pi \hbar} \mu_0 \left(\frac{m_b^*}{m_e}\right)^{1/2} \tag{B5}$$

$$\sigma_{E_0,2D} = \frac{8e m_e k_B T}{\pi a \hbar^2} \mu_0 \left(\frac{m_b^*}{m_e}\right) \tag{B6}$$

$$\sigma_{E_0,3D} = \frac{4e\left(2m_e k_B T\right)^{3/2}}{3\pi^2 \hbar^3} \mu_0 \left(\frac{m_b^*}{m_e}\right)^{3/2} \tag{B7}$$

Because we assume $N_V = 4$ for the 3D pockets at L in PbTe, we can rewrite equation B7 in terms of m_{DOS}^*, where $m_{DOS}^* = m_b^* 4^{2/3}$.

$$\sigma_{E_0,3D} = \frac{e\left(2m_e k_B T\right)^{3/2}}{3\pi^2 \hbar^3} \mu_0 \left(\frac{m_{DOS}^*}{m_e}\right)^{3/2} \tag{B8}$$

In Eq. B8, the term, $\mu_0 \left(\frac{m_{DOS}^*}{m_e}\right)^{3/2}$, is the weighted mobility, μ_w, for the 3D effective mass model.[6,9,15] Therefore, we can rewrite $\sigma_{E_0,3D}$ in terms of μ_w.

$$\sigma_{E_0,3D} = \frac{e\left(2m_e k_B T\right)^{3/2}}{3\pi^2 \hbar^3} \mu_w \tag{B9}$$

It is instructive to rewrite Eqs. B5-B7 in terms of the hole concentration (Eqs. 32-34 in the main text).

$$\sigma_{E_0,1D} = \frac{2}{3} \frac{p_{1D} e \mu_0}{F_{-\frac{1}{2}}(\eta)} \tag{B10}$$

$$\sigma_{E_0,2D} = \frac{2}{3} \frac{p_{2D} e \mu_0}{F_0(\eta)} \tag{B11}$$

$$\sigma_{E_0,3D} = \frac{2}{3} \frac{p_{3D} e \mu_0}{F_{\frac{1}{2}}(\eta)} \tag{B12}$$

Using Eq. B4 along with Eqs. B10-B12, the electrical conductivity for each case can be expressed as follows.

$$\sigma_{1D} = \frac{2 p_{1D} e \mu_0}{3} \left(r + \frac{1}{2}\right) \frac{F_{r-\frac{1}{2}}(\eta)}{F_{-\frac{1}{2}}(\eta)} \tag{B13}$$

$$\sigma_{2D} = \frac{2p_{2D}e\mu_0}{3}\,(r+1)\,\frac{F_r(\eta)}{F_0(\eta)} \tag{B14}$$

$$\sigma_{3D} = \frac{2p_{3D}e\mu_0}{3}\left(r+\frac{3}{2}\right)\frac{F_{r+\frac{1}{2}}(\eta)}{F_{\frac{1}{2}}(\eta)} \tag{B15}$$

If we use the acoustic-phonon approximation for scattering time, these equations can be simplified, as shown below.

$$\sigma_{1D} = \frac{2p_{1D}e\mu_0}{3}\frac{F_0(\eta)}{F_{-\frac{1}{2}}(\eta)} \tag{B16}$$

$$\sigma_{2D} = \frac{2p_{2D}e\mu_0}{3} \tag{B17}$$

$$\sigma_{3D} = \frac{2p_{3D}e\mu_0}{3}\frac{F_0(\eta)}{F_{\frac{1}{2}}(\eta)} \tag{B18}$$

If we were to use the constant scattering time approximation ($r = 0$), it would be more evident that on a given point of the Fermi surface, the charge carriers in the 1D case can only travel in one of the three directions, that the charge carriers of the 2D topology can move in two of the three directions, and that they can transport in all directions in the 3D case. That is, we can write the electrical conductivity for these three cases as $\sigma_{1D} = (1/3)p_{1D}e\mu_0$, $\sigma_{2D} = (2/3)p_{2D}e\mu_0$, and $\sigma_{3D} = p_{3D}e\mu_0$.

B.3 Seebeck Coefficient, S

The general expression for the Seebeck coefficient, S given by the BTE is expressed in Eq. B19.

$$S(T) = \left(\frac{k_B}{e}\right)\frac{\int \sigma(\varepsilon)\left(-\frac{df}{d\varepsilon}\right)(\varepsilon-\eta)d\varepsilon}{\int \sigma(\varepsilon)\left(-\frac{df}{d\varepsilon}\right)d\varepsilon} \tag{B19}$$

This can be reduced to Eqs. B20-B22 for the 1D-3D bands.

$$S_{1D} = \left(\frac{k_B}{e}\right)\left[\frac{\left(r+\frac{3}{2}\right)F_{r+\frac{1}{2}}(\eta)}{\left(r+\frac{1}{2}\right)F_{r-\frac{1}{2}}(\eta)} - \eta\right] \tag{B20}$$

$$S_{2D} = \left(\frac{k_B}{e}\right)\left[\frac{(r+2)\,F_{r+1}(\eta)}{(r+1)\,F_r(\eta)} - \eta\right] \tag{B21}$$

$$S_{3D} = \left(\frac{k_B}{e}\right)\left[\frac{\left(r+\frac{5}{2}\right)F_{r+\frac{3}{2}}(\eta)}{\left(r+\frac{3}{2}\right)F_{r+\frac{1}{2}}(\eta)} - \eta\right] \tag{B22}$$

When the acoustic-phonon scattering approximation is used, these expressions reduce to that found in in Eq. 28 for all three dimensionalities.

B.4 Lorenz number, L

The electronic component of the lattice thermal conductivity can be expressed as $\kappa_e = L\sigma T$, where L is the Lorenz number, given in by $L = \frac{\kappa_0}{\sigma T} - S^2$. The expression for κ_0 is given in Eq. B23.[87,96]

$$\kappa_0(T) = T\left(\frac{k_B}{e}\right)^2 \int (\varepsilon-\eta)^2 \sigma(\varepsilon)\left(-\frac{df}{d\varepsilon}\right) d\varepsilon \tag{B23}$$

Therefore, the Lorentz factor can be written in the forms shown in Eq. B24-B26.

$$L_{1D} = \left(\frac{k_B}{e}\right)^2 \frac{\left(r+\frac{5}{2}\right)\left(r+\frac{1}{2}\right)F_{r+\frac{3}{2}}(\eta)F_{r-\frac{1}{2}}(\eta) - \left(r+\frac{3}{2}\right)^2 F^2_{r+\frac{1}{2}}(\eta)}{\left(r+\frac{1}{2}\right)^2 F^2_{r-\frac{1}{2}}(\eta)} \tag{B24}$$

$$L_{2D} = \left(\frac{k_B}{e}\right)^2 \frac{(r+3)(r+1)F_{r+2}(\eta)F_r(\eta) - (r+2)^2 F^2_{r+1}(\eta)}{(r+1)^2 F^2_r(\eta)} \tag{B25}$$

$$L_{3D} = \left(\frac{k_B}{e}\right)^2 \frac{\left(r+\frac{7}{2}\right)\left(r+\frac{3}{2}\right)F_{r+\frac{5}{2}}(\eta)F_{r+\frac{1}{2}}(\eta) - \left(r+\frac{5}{2}\right)^2 F^2_{r+\frac{3}{2}}(\eta)}{\left(r+\frac{3}{2}\right)^2 F^2_{r+\frac{1}{2}}(\eta)} \tag{B26}$$

If we use the acoustic-phonon scattering approximation, all three of the above expressions reduce to the equation for L given in Eq. 29 of the main text.

B.5 Quality Factor, B, and Figure of Merit, zT

In general, the zT for this effective-mass model in all three cases can be calculated using Eqs. B27-B29.

$$zT_{1D}(\eta, B) = \frac{S^2(\eta)}{\frac{(k_B/e)^2}{(r+1/2)B_{1D}F_{r-\frac{1}{2}}(\eta)} + L(\eta)} \tag{B27}$$

$$zT_{2D}(\eta, B) = \frac{S^2(\eta)}{\frac{(k_B/e)^2}{(r+1)B_{2D}F_r(\eta)} + L(\eta)} \tag{B28}$$

$$zT_{3D}(\eta, B) = \frac{S^2(\eta)}{\frac{(k_B/e)^2}{(r+3/2)B_{3D}F_{r+\frac{1}{2}}(\eta)} + L(\eta)} \tag{B29}$$

The quality factor, B, is defined in terms of σ_{E_0} in Eq. B30[6,15]. For each topology, the quality factory is calculated from the corresponding σ_{E_0}.

$$B = \left(\frac{k_B}{e}\right)^2 \frac{\sigma_{E_0} T}{\kappa_L} \tag{B30}$$

For the acoustic-phonon scattering assumption used in this paper, the zT's for the 1D, 2D, and 3D PbTe bands are identical, and given in Eq. 30 of the main text.

C Bandgap Energy from Tight-Binding Model

PbTe has a direct bandgap at L,[40–42,45,66,97,98] so an analytical expression for the bandgap energy of PbTe can be found simply by subtracting the analytical solutions of the VBM from the CBM. If we do not include SOC, we can find exact analytical solutions to the tight-binding eigenvalues that represent the VBM and CBM.

The solution for the VBM state is given in Eq. 2 in the main text. The expression for the CBM, $E_{CBM}(\mathrm{L})$ is analogous except the anion and cation orbitals interactions are flipped. Here, we must distinguish between the two nearest-neighbor $V_{sp\sigma}$ in the same manner as in Appendix A, where $V_{sp\sigma 1}$ refers to cation-s/anion-p interactions, and $V_{sp\sigma 2}$ refers to anion-s/cation-p interactions. Using this notation, we can express the CBM energy as follows:

$$E_{CBM}(\mathrm{L}) = \frac{1}{2}\left(E_{s,Te} + E'_{p,Pb}(\mathrm{L})\right) + \frac{1}{2}\sqrt{\left(E'_{p,Pb}(\mathrm{L}) - E_{s,Te}\right)^2 + 48V_{sp\sigma 2}^2} \tag{C1}$$

$$E'_{p,Pb}(\mathrm{L}) = E_{p,Pb} + 4V_{pp\pi,Pb} - 4V_{pp\sigma,Pb} \tag{C2}$$

Therefore, the bandgap energy, E_g, can be written in the form below.

$$\begin{aligned} E_g = {} & \frac{1}{2}\left(E_{s,Te} - E_{s,Pb} + E_{p,Pb} - E_{p,Te} - 4V_{pp,Pb} + 4V_{pp,Te}\right) + \\ & \frac{1}{2}\left(\sqrt{\left(E_{p,Pb} - E_{s,Te} - 4V_{pp,Pb}\right)^2 + 48V_{sp\sigma 2}^2} - \sqrt{\left(E_{p,Te} - E_{s,Pb} - 4V_{pp,Te}\right)^2 + 48V_{sp\sigma 1}^2}\right) \end{aligned} \tag{C3}$$

$V_{pp,Pb}$ describes the strength of the cation-p interactions and is defined through the expression, $V_{pp,Pb} = V_{pp\sigma,Pb} - V_{pp\pi,Pb}$. From Eq. C3, we see that the bandgap energy increases as (1) $V_{sp\sigma 1}$

(cation-s, anion-p) decreases, (2) $V_{sp\sigma 2}$ (anion-s, cation-p) increases, (3) the difference in on-site energies between the cation-s and anion-p states increases, (4) the energy splitting between the anion-s and cation-p states decrease, (5) the anion-p interactions are strengthened ($V_{pp,Te}$ increases), and (6) the cation-p interactions are weakened ($V_{pp,Pb}$ decreases).

While the above equation allows us to determine trends in E_g with respect to TB orbital interactions and on-site energies, it is expected to significantly overestimate the bandgap, as SOC interactions are not considered. When SOC interactions are included, the bandgap energy decreases.[41,66,88,89,97,99]. We can also relate some of the trends in bandgap energy to the convergence trends discussed in the main text. For example, decreasing $V_{sp\sigma 1}$, increasing the on-site energy difference between the cation-s and anion-p states, and increasing $V_{pp,Te}$ all increase the bandgap and converge the VB extrema.

D Labeled First Brillouin Zone for the FCC Lattice

Fig. D1 depicts the first Brillouin Zone (BZ) for the face-centered cubic (FCC) lattice with high-symmetry points labeled.[68] The red cube with red lines across the two diagonals of each face is included as a visual guide. The points Σ' and Δ' are not conventional high-symmetry points and are defined specifically for the purposes of this study. We define these points (and the other conventional high-symmetry points) at follows, where a is the lattice parameter:

- $\Gamma = (0, 0, 0)$
- $\Sigma' = \left(\frac{\pi}{a}, \frac{\pi}{a}, 0\right)$
- $\Delta' = \left(\frac{\pi}{a}, 0, 0\right)$
- $\mathrm{L} = \left(\frac{\pi}{a}, \frac{\pi}{a}, \frac{\pi}{a}\right)$
- $\mathrm{X} = \left(\frac{2\pi}{a}, 0, 0\right)$
- $\mathrm{K} = \left(\frac{3\pi}{2a}, \frac{3\pi}{2a}, 0\right)$
- $\mathrm{W} = \left(\frac{2\pi}{a}, \frac{\pi}{a}, 0\right)$

There are 12 symmetrically equivalent Σ'-points, 6 symmetrically equivalent Δ'-points, 6 equivalent W–points, 4 equivalent K–points, 4 L–points, 3 X–points, and 1 Γ–point in the first BZ.

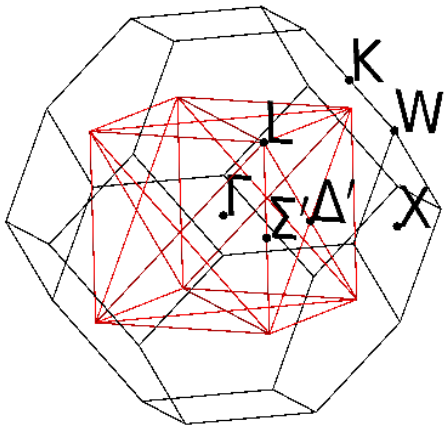

Figure D1: Labeled first Brillouin zone (BZ) of an FCC lattice. A red cube with red lines across the two diagonals of each of the 6 faces is included as a visual guide. The cube has a side length of $2\pi/a$, where a is the lattice parameter. The Γ-point is at the center of the cube and BZ, the L-point is at the corner of the red cube and at the center of the hexagonal face of the BZ, the X-point is in the center of the square face of the BZ, the W-point is on the corners of the BZ faces, the K-point is found on the edge-centers of the hexagonal first BZ faces, and the Σ'-point is located at the center of the edges of the red cube. The Δ'-point is at the center of the faces of the red cube, exactly halfway between Γ and X.